Baryon acoustic oscillations in the projected cross-correlation function between the eBOSS DR16 quasars and photometric galaxies from the DESI Legacy Imaging Surveys

Pauline Zarrouk,[1]* Mehdi Rezaie [iD],[2] Anand Raichoor,[3] Ashley J. Ross [iD],[4] Shadab Alam,[5] Robert Blum,[6] David Brookes,[7] Chia-Hsun Chuang [iD],[8] Shaun Cole,[1] Kyle S. Dawson,[9] Daniel J. Eisenstein,[10] Robert Kehoe,[11] Martin Landriau,[12] John Moustakas,[13] Adam D. Myers,[14] Peder Norberg,[1,15] Will J. Percival,[16,17] Francisco Prada,[18] Michael Schubnell,[19] Hee-Jong Seo [iD],[2] Gregory Tarlé[19] and Cheng Zhao [iD][20]

[1]*Institute for Computational Cosmology, Department of Physics, Durham University, South Road, Durham DH1 3LE, UK*
[2]*Department of Physics and Astronomy, Ohio University, 251B Clippinger Labs, Athens, OH 45701, USA*
[3]*Institute of Physics, Laboratory of Astrophysics, École Polytechnique Fédérale de Lausanne (EPFL), Observatoire de Sauverny, CH-1290 Versoix, Switzerland*
[4]*Center for Cosmology and Astro-Particle Physics, Ohio State University, Columbus, OH 43210, USA*
[5]*Institute for Astronomy, University of Edinburgh, Royal Observatory, Blackford Hill, Edinburgh EH9 3HJ, UK*
[6]*National Optical Astronomy Observatory, 950 N. Cherry Ave., Tucson, AZ 85719, USA*
[7]*Department of Physics and Astronomy, University College London, Gower Street, London WC1E 6BT, UK*
[8]*Kavli Institute for Particle Astrophysics and Cosmology, Stanford University, 452 Lomita Mall, Stanford, CA 94305, USA*
[9]*Department of Physics and Astronomy, University of Utah, Salt Lake City, UT 84112, USA*
[10]*Harvard–Smithsonian Center for Astrophysics, 60 Garden St, Cambridge, MA 02138, USA*
[11]*Department of Physics, Southern Methodist University, 3215 Daniel Ave., Dallas, TX 75205, USA*
[12]*Lawrence Berkeley National Laboratory, 1 Cyclotron Road, Berkeley, CA 94720, USA*
[13]*Department of Physics and Astronomy, Siena College, 515 Loudon Road, Loudonville, NY 12211, USA*
[14]*Department of Physics and Astronomy, University of Wyoming, Laramie, WY 82071, USA*
[15]*Centre for Extragalactic Astronomy, Department of Physics, University of Durham, South Road, Durham DH1 3LE, UK*
[16]*Waterloo Centre for Astrophysics, University of Waterloo, 200 University Ave. W, Waterloo, ON N2L 3G1, Canada*
[17]*Department of Physics and Astronomy, University of Waterloo, 200 University Ave. W, Waterloo, ON N2L 3G1, Canada*
[18]*Instituto de Astrofsica de Andaluca (CSIC), Glorieta de la Astronoma, s/n, E-18008 Granada, Spain*
[19]*Department of Physics, University of Michigan, Ann Arbor, MI 48109, USA*
[20]*Institute of Physics, Laboratory of Astrophysics, École Polytechnique Fédérale de Lausanne (EPFL), Observatoire de Sauverny, CH-1290 Versoix, Switzerland*

ABSTRACT
We search for the baryon acoustic oscillations in the projected cross-correlation function binned into transverse comoving radius between the SDSS-IV DR16 eBOSS quasars and a dense photometric sample of galaxies selected from the DESI Legacy Imaging Surveys. We estimate the density of the photometric sample of galaxies in this redshift range to be about 2900 deg^{-2}, which is deeper than the official DESI emission line galaxy selection, and the density of the spectroscopic sample is about 20 deg^{-2}. In order to mitigate the systematics related to the use of different imaging surveys close to the detection limit, we use a neural network approach that accounts for complex dependences between the imaging attributes and the observed galaxy density. We find that we are limited by the depth of the imaging surveys that affects the density and purity of the photometric sample and its overlap in redshift with the quasar sample, which thus affects the performance of the method. When cross-correlating the photometric galaxies with quasars in the range $0.6 \leq z \leq 1.2$, the cross-correlation function can provide better constraints on the comoving angular distance $D_{\rm M}$ (6 per cent precision) compared to the constraint on the spherically averaged distance $D_{\rm V}$ (9 per cent precision) obtained from the autocorrelation. Although not yet competitive, this technique will benefit from the arrival of deeper photometric data from upcoming surveys that will enable it to go beyond the current limitations we have identified in this work.

Key words: cosmology: observations – dark energy – distance scale.

* E-mail: pauline.s.zarrouk@durham.ac.uk

1 INTRODUCTION

The baryon acoustic oscillations (BAO) feature (Cole et al. 2005; Eisenstein et al. 2005) in the clustering of galaxies left by the baryon–photon plasma that propagated as sound waves until decoupling in the early Universe has emerged as a very robust way of measuring cosmic distances across time. The BAO measurement in samples of galaxies at different redshifts is a powerful geometrical test to probe the expansion history of the Universe in a complementary way to cosmic microwave background anisotropies (Planck Collaboration VI 2020) and to the Hubble diagram with Type Ia supernovae for the local Universe, such as the recent *HST* programme SH0ES (Riess et al. 2018, 2019) and the Carnegie-Chicago Hubble programme (Freedman et al. 2019). These various cosmological data sets have shown increasing evidence that the cosmic expansion has been accelerating for 6 billion yr. However, the mechanism that is driving such an acceleration is one of the biggest mysteries in cosmology. It is commonly known as 'dark energy' where, in the standard cosmological model, we introduce the cosmological constant Λ that could be associated with vacuum energy to account for this late-time acceleration. The current observations could also be explained by more complex dark energy models with time-dependent properties or even a modification of general relativity at cosmological scales (e.g. Linder & Cahn 2007; Guzzo et al. 2008).

Ongoing and planned cosmic surveys have been designed to distinguish between these possibilities and more generally to test the standard model of cosmology, Lambda cold dark matter (ΛCDM). Dense spectroscopic samples of large-scale structure tracers are required to measure the BAO feature accurately, but it becomes observationally expensive especially at high redshifts ($z \geq 1$) where galaxies are fainter and less abundant. Bright galaxies such as the BOSS luminous red galaxies (BOSS LRGs; Alam et al. 2017) have been extensively probed by spectroscopic surveys to reconstruct the map of the large-scale structures of the Universe up to $z < 0.6$. The SDSS-IV eBOSS programme (Dawson et al. 2016) undertook a survey of emission line galaxies (ELGs) and quasars to probe the unexplored intermediate redshift range ($0.6 < z < 2.2$) and set the scene for the advent of Stage IV dark energy experiments including the Dark Energy Spectroscopic Instrument at the Kitt Peak Observatory (DESI Collaboration 2016a, b), the space mission *Euclid* (Amendola et al. 2013), and the Legacy Survey of Space and Time at the Vera C. Rubin Observatory (LSST Dark Energy Science Collaboration 2012). Current and upcoming galaxy surveys are also providing larger and larger samples of photometric data. Attempts to measure the BAO feature in the correlation function of photometric galaxy samples (Padmanabhan et al. 2007; Ross, Percival & Manera 2015) continue improving with the ongoing generation of surveys like Hyper-Suprime Camera (HSC; Aihara et al. 2018), the Dark Energy Survey (DES Collaboration 2018), and the Kilo-Degree Survey (KIDS; de Jong et al. 2015). However, the photometric BAO analysis is based on the angular correlation function of galaxies that loses the clustering information along the line-of-sight direction due to projection. It thus mixes different physical scales, which leads to a smearing of the BAO feature and to a loss of precision in the cosmological constraints.

On the one hand, spectroscopic data provide accurate redshift measurements but are limited by the statistics at high redshift ($z > 1$). On the other hand, samples of photometric data are much larger but with less precise information in the radial direction. Therefore, exploiting the cross-correlation between both types of data has been more and more used, mainly in order to characterize the properties of the photometric data set. For instance, Padmanabhan et al. (2009)

studied the small-scale clustering of a sample of photometrically selected LRGs using a spectroscopic sample of quasars in the range $0.2 < z < 0.6$. Methods to infer the redshift distribution of a photometric sample by measuring the amplitude of cross-correlation with spectroscopic samples have been developed (for a review, see Newman 2008) and this technique has been recently applied to the photometric sample of DESI LRGs and was able to recover the expected redshift distribution (Kitanidis et al. 2020). Another application of such kind of cross-correlation was proposed by Patej & Eisenstein (2018) with the goal of improving the BAO measurement in a sparse spectroscopic sample by exploiting the cross-correlation with a denser photometric sample. Nishizawa, Oguri & Takada (2013) already showed that the measurement of the correlation function as a function of transverse comoving radius rather than angular separation preserves the BAO scale inherent in the large-scale structures. Then, Patej & Eisenstein (2018) derived the analytical prediction in configuration space and they presented a proof of concept that the BAO scale could be measured in the cross-correlation function binned by transverse comoving radius.

In this paper, we develop and apply this method to measure the BAO feature in the projected cross-correlation of eBOSS DR16 quasars and a photometric sample of galaxies selected from the DESI Legacy Imaging Surveys (Dey et al. 2019). We perform two analyses in parallel, one from the autocorrelation function of the eBOSS DR16 quasars and one from the projected cross-correlation function, both under the same fitting conditions. By providing a proper comparison between the two statistics, our goal is to highlight the potential benefit of using the cross-correlation between photometry and spectroscopy for BAO measurement. The paper is structured as follows. Section 2 presents the analytical prediction for the projected cross-correlation function. Then, we present the spectroscopic and photometric data sets in Section 3 and the methodology for this analysis in Section 4. Eventually, the measurements and results are shown and discussed in Section 5 followed by the conclusion in Section 6.

2 BAO IN THE PROJECTED CROSS-CORRELATION FUNCTION

2.1 Transverse comoving separation

Instead of considering angular separation between a spectroscopic object and the surrounding photometric galaxies, the key idea is to consider the cross-correlation binned by transverse comoving separation where photometric galaxies are assumed to be at the same redshift as the spectroscopic object they are correlated with. The transverse separation **R** is thus defined in terms of observed angular positions and the comoving angular diameter distance evaluated at the spectroscopic redshift $D_M(z_s)$:

$$\mathbf{R} = D_M(z_s)\arccos(\boldsymbol{\gamma}_s \cdot \boldsymbol{\gamma}_p) = D_M(z_s)|\boldsymbol{\theta}_s - \boldsymbol{\theta}_p|, \qquad (1)$$

where the unit vector on the celestial sphere $\boldsymbol{\gamma}$ is defined by $\boldsymbol{\gamma} = (\sin\theta\cos\phi, \sin\theta\sin\phi, \cos\theta)$ and $\boldsymbol{\theta}_s$ ($\boldsymbol{\theta}_p$) is the angular separation between the spectroscopic quasar (the photometric galaxy) and the line-of-sight direction. We assume the sky is locally flat over separations between correlated galaxies.

The conversion from angular position to transverse comoving separation assumes a fiducial cosmological model, and also in the next section, we will assume a linear matter power spectrum. We use a flat ΛCDM cosmological model with the following parameters:

$$h = 0.676, \ \Omega_m = 0.31, \ \Omega_\Lambda = 0.69,$$
$$\Omega_b h^2 = 0.022, \ m_\nu = 0.06 \text{ eV}, \ \sigma_8 = 0.80. \qquad (2)$$

where the subscripts m, b, and ν stand for matter, baryon, and neutrino, respectively, and h is the standard dimensionless Hubble parameter. These choices match the fiducial cosmology adopted for the BAO analysis of the eBOSS quasar sample DR14 (Ata et al. 2018) and DR16 (Neveux et al. 2020; Hou et al. 2021).

2.2 Analytical projected cross-correlation function

Patej & Eisenstein (2018) detailed the mathematical formalism associated with the projected cross-correlation function $w_\theta(\mathbf{R})$. In this section, we just recall the most important steps in obtaining an analytical prediction for $w_\theta(\mathbf{R})$. The spectroscopic sample is characterized by an overdensity field $\delta_s(\mathbf{r})$ and the photometric sample by a projected overdensity field $\Delta_p(\boldsymbol{\theta})$ defined as

$$\Delta_p(\boldsymbol{\theta}) = \frac{\int r^2 n_p(r)\delta_p(\mathbf{r})\mathrm{d}r}{\int r^2 n_p(r)\mathrm{d}r}, \tag{3}$$

where $n_p(r)$ is the number density of photometric galaxies and $\delta_p(\mathbf{r})$ the overdensity field associated with the photometric sample.

The projected cross-correlation function $w_\theta(\mathbf{R})$ is then:

$$w_\theta(\mathbf{R}) = \langle \delta_s(\mathbf{r})\Delta_p(\boldsymbol{\theta} + \mathbf{R}/r) \rangle, \tag{4}$$

where the transverse comoving separation $\mathbf{R}$ is defined by equation (1) and $\mathbf{r} = (r, \boldsymbol{\theta})$.

Using the flat-sky approximation, Patej & Eisenstein (2018) derived a detailed analytical expression in agreement with Padmanabhan et al. (2009) who first showed that the projected correlation function binned by physical transverse separation $w_\theta(\mathbf{R})$ can be related to the standard projected correlation $w_p(\mathbf{R})$ (Davis & Peebles 1983) by

$$w_\theta(\mathbf{R}) = \langle f(b_s, n_s, b_p, n_p) \rangle w_p(\mathbf{R}) \tag{5}$$

where $\langle f(\chi) \rangle$ scales the amplitude of the standard projected cross-correlation function according to the overlap in redshift between the photometric galaxies and the spectroscopic quasars they are correlated with. This factor is defined in Patej & Eisenstein (2018) as follows:

$$\langle f(b_s, n_s, b_p, n_p) \rangle = \frac{b_s b_p}{2\pi} \frac{\int \mathrm{d}r\, r^2 n_s(r)W(r,\eta)n_p(r)}{\int \mathrm{d}r\, n_s(r)W(r,\eta) \int \mathrm{d}r'\, r'^2 n_p(r')}, \tag{6}$$

where b_s is the linear bias of the spectroscopic sample, b_p is the linear bias of the photometric sample, n_s is the redshift-dependent mean number density of the spectroscopic sample, n_p is the redshift-dependent mean number density of the photometric sample, and $W(r, \eta)$ is a weighting function that accounts for selection effects and can depend on r and other variables that are collectively referred to as η. However, so far in the clustering analyses, the weights that have been derived do not depend on r or η and we generally assume that the linear biases are scale-independent, therefore equation (6) can be seen as a normalization factor that will be fitted to the data. If the two redshift distributions were overlapping perfectly, the second ratio would be equal to 1 and the normalization factor would simply be $b_s b_p / 2\pi$.

The standard projected correlation function $w_p(\mathbf{R})$ can be calculated as the line-of-sight integral of the 2D power spectrum defined as

$$w_p(\mathbf{R}) = \frac{1}{2\pi} \int \mathrm{d}^2 k_\perp P(k_\perp) e^{i\mathbf{k}_\perp \cdot \mathbf{R}}, \tag{7}$$

where $k = \sqrt{k_\parallel^2 + k_\perp^2} \approx k_\perp$ assuming that the range of the line-of-sight distance projected over is much larger than the BAO scale.
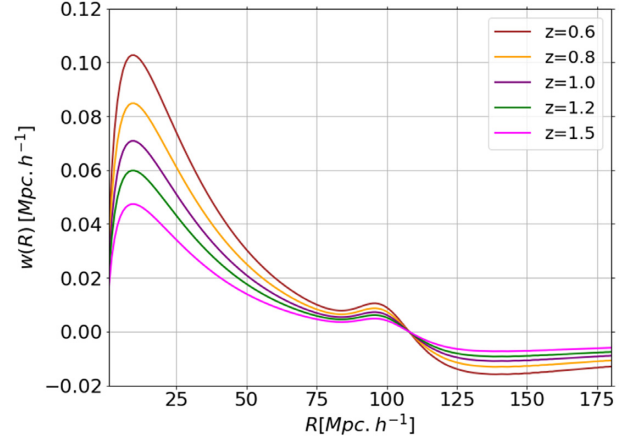

Figure 1. Evolution with redshift of the template for the matter projected correlation function following equation (9) and with a bin width of $1\,h^{-1}$ Mpc.

However, the expectation value derived for $w_\theta(\mathbf{R})$ in equation (5) only holds for a single separation $\mathbf{R}$ whereas the data are binned. So to account for this binning, one can exploit that the clustering depends only on r due to isotropy. Therefore, by integrating over circular annuli with bounds R_1 and R_2, we can obtain the following binned correlation function:

$$w(R_1, R_2) = 2 \int_{R_1}^{R_2} \frac{R\mathrm{d}R}{(R_2^2 - R_1^2)} \int \frac{\mathrm{d}\phi}{2\pi} w_\theta(\mathbf{R}), \tag{8}$$

which then leads to equation (80) of Patej & Eisenstein (2018):

$$w(R_1, R_2) = \frac{b_s b_p}{2\pi^2(R_2^2 - R_1^2)} \frac{\int \mathrm{d}r\, r^2 n_s(r)W(r,\eta)n_p(r)}{\int \mathrm{d}r\, n_s(r)W(r,\eta) \int \mathrm{d}r'\, r'^2 n_p(r')}$$
$$\times \int \mathrm{d}^2 k_\perp P(k_\perp) \frac{R_2 J_1(k_\perp R_2) - R_1 J_1(k_\perp R_1)}{k_\perp}. \tag{9}$$

This is the analytical expression we will use to fit to the data in Section 5.2.2.

2.3 Implicit assumptions

The above derivation implicitly assumes that $w_p(\mathbf{R})$ does not vary across the redshift range of interest. Of course, this is not true and Fig. 1 shows the redshift evolution of the matter projected cross-correlation function using equation (9) for a bin width of $1\,h^{-1}$ Mpc. However, in the context of BAO measurements, we argue that the position of the BAO peak is not affected and any modification of the shape of the projected cross-correlation can be accounted for with the bias and broad-band parameters. Nevertheless, in Section 4.4, we propose three assumptions for the redshift distribution of the photometric sample that can affect the effective redshift definition and in Section 5.2.2, we will show the impact on the BAO measurements.

Another assumption is related to the input matter power spectrum $P(k_\perp)$ that enters equation (9). We generate it using CAMB (Lewis, Challinor & Lasenby 2000) assuming a linear prediction. We have checked that including non-linear corrections from the Halofit model (Smith et al. 2003; Takahashi et al. 2012) in CAMB has a marginal effect on small scales ($R \leq 20\,h^{-1}$ Mpc). Moreover, the projected clustering is less affected by redshift-space distortions, RSD (Ross et al. 2011) and we do not use photometric redshifts to locate the position of the galaxies along the line of sight. So we expect the RSD correction to be negligible. Eisenstein, Seo & White (2007) showed that non-linearities can also lead to a broadening of the BAO peak. However, this evolution is sufficiently slow that
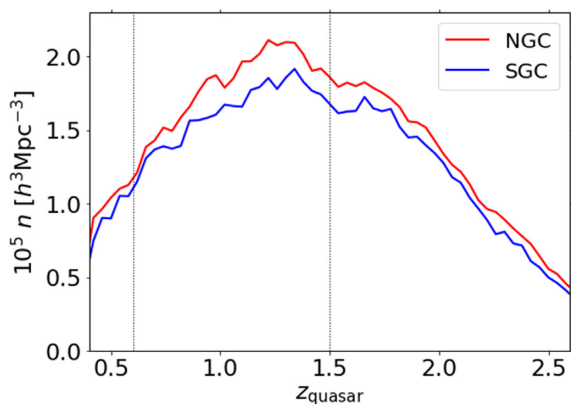
Figure 2. Redshift distribution of the spectroscopic eBOSS quasars. We keep quasars in $0.6 \leq z \leq 1.5$ only as indicated by the dotted lines.

it can be accounted for by adding a damping term in the BAO template. Eventually, we can also have a scale-dependent bias that becomes important at small scales. In a BAO analysis, however, this is usually accounted for by the broad-band parameters. We refer to Section 4.3 where we present the BAO fitting procedure and introduce the damping term and the broad-band parameters.

3 DATA

3.1 Spectroscopic data set

As highlighted in Patej & Eisenstein (2018), the cross-correlation method described above is expected to reduce shot noise and to improve the BAO measurement in a sparse spectroscopic sample. Actually, the SDSS-IV eBOSS quasars represent a sparse spectroscopic sample with $nP_0 = 0.12 < 1$ where $n \simeq 10^{-4} \, h^{-3} \, \mathrm{Mpc}^{-3}$ is the quasar density (which is about an order of magnitude lower than for galaxies) and $P_0 = 6000 \, h^{-3} \, \mathrm{Mpc}^3$ is the typical amplitude of the quasar power spectrum at the BAO scale.

Our analysis uses the CORE spectroscopic sample of quasars obtained by the SDSS-IV eBOSS programme (Dawson et al. 2016) using the 2.5-m Sloan Foundation telescope (Gunn et al. 2006) at the Apache Point Observatory with the same two-arm optical fibre-fed spectrographs as BOSS (Smee et al. 2013). The CORE quasar target selection (Myers et al. 2015) is based on the SDSS-I-II-III optical imaging data in the *ugriz* (Fukugita et al. 1996) bands and on the imaging data from the Wide-field Infrared Survey Explorer (*WISE*; Wright et al. 2010). Selection is performed using a likelihood-based routine called the 'Extreme Deconvolution' algorithm (XDQSO) in order to obtain a homogeneous quasar sample at $g < 21$. The algorithm has been improved for eBOSS with XDQSOz (Bovy et al. 2012) so that it can be applied to any redshift range. The spectroscopic sample used in this analysis is obtained with the same methodology as for the large-scale structure DR16 eBOSS quasar catalogue (Ross et al. 2020) but instead of considering quasars between $0.8 \leq z \leq 2.2$, we use quasars between $0.6 \leq z \leq 1.5$. Including quasars at $z < 0.8$ and removing those at $z > 1.5$ allows us to increase the overlap in redshift with the sample of photometric galaxies. There are very few quasars below $z = 0.6$ and few photometric galaxies above $z = 1.5$. The photometric sample is described in the next section. The redshift distribution of the eBOSS DR16 quasar catalogue (Lyke et al. 2020) is shown in Fig. 2 in blue for the Northern Galactic cap (NGC) and red for the Southern Galactic cap (SGC). The dotted vertical lines delineate our range $0.6 < z < 1.5$.
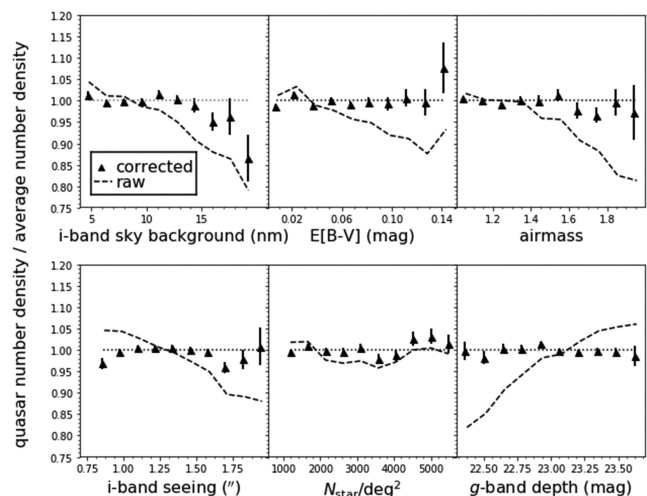

Figure 3. Quasar target density variation with imaging systematics before (raw data as dotted lines) and after applying weights to correct for the variation with g-band depth and Galactic extinction (E[B − V]). Here, we consider quasars in $0.6 \leq z \leq 1.5$.

As in Ross et al. (2020), we apply a cut in the completeness per sector where we restrict to sectors that have $C_{\mathrm{eBOSS}} > 0.5$ such that the completeness of the quasar sample is ~ 97.7 per cent. We also correct for any missing targets or spurious correlation in the target density by applying several weights to the data and the randoms following Ross et al. (2020):

(i) Systematics weights w_{sys} are used to correct for inhomogeneities in the quasar density due to variations in the quality of the SDSS photometry. Such variations can lead to angular variations of the depth (5σ detection in magnitude for a point-source object) that also depend on the airmass, seeing, and Galactic extinction. We compute systematics weights for the NGC and SGC separately based on linear regression according to the dependence of the quasar density on the SDSS imaging depth in the g-band, Galactic extinction, the seeing, and the sky background. The procedure was identical to that described in Ross et al. (2020), except for the $0.6 < z < 1.5$ redshift range. Fig. 3 displays the target density variation with the imaging systematics before applying the correction with depth and Galactic extinction (raw data) and after (corrected). We then correct for the remaining dependence on seeing and sky background.

(ii) Close-pairs (fibre-collisions) weights w_{cp} are used to account for the missing targets in a collision group due to the finite size of a spectroscopic fibre that prevents observing two quasars within a radius of 62 arcsec. We compute weights that are assigned and equally distributed per collision group.

(iii) Redshift failures weights w_{noz} are used to account for the missing targets due to invalid redshifts that we correct for by computing weights based on the spectrograph signal to noise in the i-band and the fibre ID.

(iv) FKP weight w_{FKP} (Feldman, Kaiser & Peacock 1994) is used to minimize the variance of the measurement and is defined by $w_{\mathrm{FKP}} = (1 + P_0 n(z))^{-1}$.

The total weight that is applied to the data and the random is thus defined by

$$w_{\mathrm{tot}} = w_{\mathrm{FKP}} \cdot w_{\mathrm{sys}} \cdot w_{\mathrm{cp}} \cdot w_{\mathrm{noz}} \qquad (10)$$

3.2 Photometric data set

In order to maximize the cross-correlation signal, we need to select photometric galaxies in the same footprint but also in the same redshift range as the spectroscopic sample. We also need to reach a sampling of galaxies dense enough such that $n_p P_p > 1$ where n_p is the density of the photometric galaxies and P_p is the typical value of the power spectrum of the photometric sample at the BAO scale. Given our choice of spectroscopic sample, we want to select photometric galaxies in the redshift range $0.6 < z < 1.5$, where star-forming galaxies are ideal candidates as they are abundant at these redshifts with strong emission lines (e.g. Madau & Dickinson 2014). Such kind of ELGs have been already observed by the SDSS-IV eBOSS programme which confirms that optical colour selection techniques can be used to optimally select ELGs in $0.6 < z < 1.1$ (Raichoor et al. 2017). The DESI instrument (DESI Collaboration 2016b) has been designed to resolve the [O II] doublet over the redshift range $0.6 < z < 1.6$ such that the ELGs constitute the largest sample of objects that DESI will observe with 28 million ELGs over 14 000 deg². We select the photometric sample using the DR8 release[1] of the DESI Legacy Imaging Surveys (Dey et al. 2019) which consist of:

(i) The Dark Energy Camera Legacy Survey (DECaLS), which provides imaging over 2/3 of the DESI footprint covering both the Northern and Southern Galactic caps (NGC and SGC) at Dec ≤ 32 deg in g, r, and z bands. It also includes the DES imaging where available.

(ii) The Beijing-Arizona Sky Survey (BASS), which observes 5500 deg² in the NGC footprint at Dec ≥ 32 deg in two optical bands (g and r). Its coverage includes 500 deg² of overlap with DECaLS in order to investigate any systematic biases in the target selection.

(iii) The Mayall z-band Legacy Survey (MzLS), which observes 5500 deg² in the NGC footprint at Dec ≥ 32 deg in the z band.

Altogether, they provide photometric data in three optical/near-infrared bands (g, r, and z) over more than 14 000 deg² with a 5σ galaxy depths of $g = 24.4$, $r = 23.8$, and $z = 23.0$. Note that the separation between BASS/MzLS and DECaLS is at Dec =32.375 deg and that this declination does not reflect the limits of the imaging but, rather, is imposed by the DESITARGET code.[2] The photometric catalogue also includes two mid-infrared bands observed by the *WISE* satellite (Wright et al. 2010). All the Legacy Imaging Surveys catalogues are built using TRACTOR[3] (Lang, Hogg & Mykytyn 2016) which is a forward-modelling algorithm to perform source extraction on pixel-level data. The footprint of the different DESI Legacy Imaging Surveys with BASS/MzLS, DECaLS, and DES together with the eBOSS footprint are shown in Fig. 4.

3.2.1 Photometric selection

Our target selection is based on three criteria: (i) clean photometry (masking around bright stars/objects and removing defective pixels), (ii) high target density, (iii) galaxies in the desired redshift range. The corresponding cuts are detailed in Table 1 and we modify the DESITARGET code[4] to implement them.

Our cuts are done on magnitudes corrected for Galactic extinction using the maps of Schlegel, Finkbeiner & Davis (1998). The
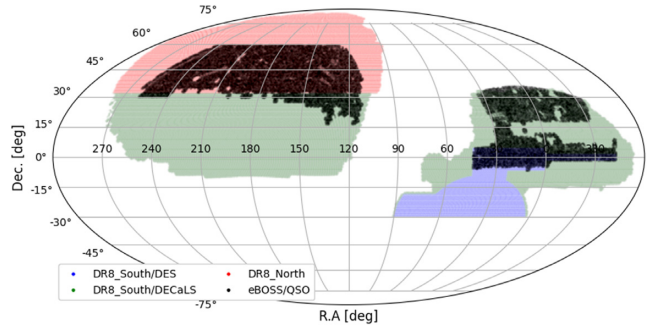

Figure 4. Footprint of the DESI Legacy Imaging Surveys with BASS/MzLS (red), DECaLS (red), and DES (blue) and of the DR16 eBOSS/QSO footprint (black).

Table 1. The ELG target selection in this study using the DESI Imaging Legacy Surveys in the NGC and SGC.

Criterion	DESI BASS/MzLS	DESI DECaLS
Clean photometry	$n_{\mathrm{obs,\ g/r/z}} > 0$, GAIA stars masking and pixel masking	
Magnitude range	$20 < g < 23.6$	$20 < g < 23.5$
Redshift range	$1.15(r-z) - 1.5 < g - r < 1.15(r-z) - 0.15$	
	$-1.2(r-z) + 1.0 < g - r < -1.2(r-z) + 2.8$	

extinction coefficients for the DECam filters are computed using *airmass* = 1.3 for a source with a 7000 K thermal spectrum as done in Schlafly & Finkbeiner (2011). These coefficients are A/E(B − V) = 3.995, 3.214, 2.165, 1.592, 1.211, 1.064 for the g, r, z, W1 and W2 bands, respectively. Galactic extinction coefficients for BASS and MzLS are also calculated as if they are on the DECam filter system. TRACTOR outputs also provide the number of observations n_{obs} in the three bands where we impose at least one observation in each band ($n_{\mathrm{obs,\ g/r/z}} > 0$), a masking around *GAIA* DR2 stars (Gaia Collaboration 2018) and corrections for instrumental effects that we call 'pixel masking'. These corrections enable us to track the pixels that have been compromised due to bad quality, saturation, cosmic rays, bleed trails, transients, edges, and outliers. They are compiled in the ALLMASK bitmask[5] and we remove those bad pixels for each band. Our pixel masking also includes pixels in the vicinity of bright stars, large galaxies[6], and globular clusters.

Fig. 5 displays the $g - r$ versus $r - z$ colour–colour diagram for galaxies in our g-band magnitude range with our selection (red box), the DESI ELG selection (black box), and the SDSS-IV eBOSS ELG selection (magenta box). The colour-coding shows the photometric redshifts of the galaxies after matching the ELG targets with HSC-PDR2 (Aihara et al. 2019). The DESI ELG target selection does not provide enough targets for this study, with a mean target density of 2400 deg^{-2} while we would like a mean density of ∼3000 deg^{-2} to have $n_p P_p \sim 5$ where we choose $P_0 = 4000\,h^{-3}$ Mpc^3 for ELGs. To reach a higher redshift density, we select less star-forming objects (i.e. with redder colours) given that we are not constrained by desiring a minimal [O II] flux as spectroscopic targets are.

Because we are only interested in the overlapping footprint with eBOSS, we apply the eBOSS geometry to the photometric sample including four veto masks for bad fields, bright objects, a centre post mask that removes the areas at the centre of the plates where no targets can be observed and a collision priority mask that removes the

---

[1] http://legacysurvey.org/dr8/description/
[2] https://github.com/desihub/desitarget/blob/master/py/desitarget/io.py#L95
[3] https://github.com/dstndstn/tractor
[4] https://github.com/desihub/desitarget/tree/master/py/desitarget

[5] http://legacysurvey.org/dr8/bitmasks/#maskbits
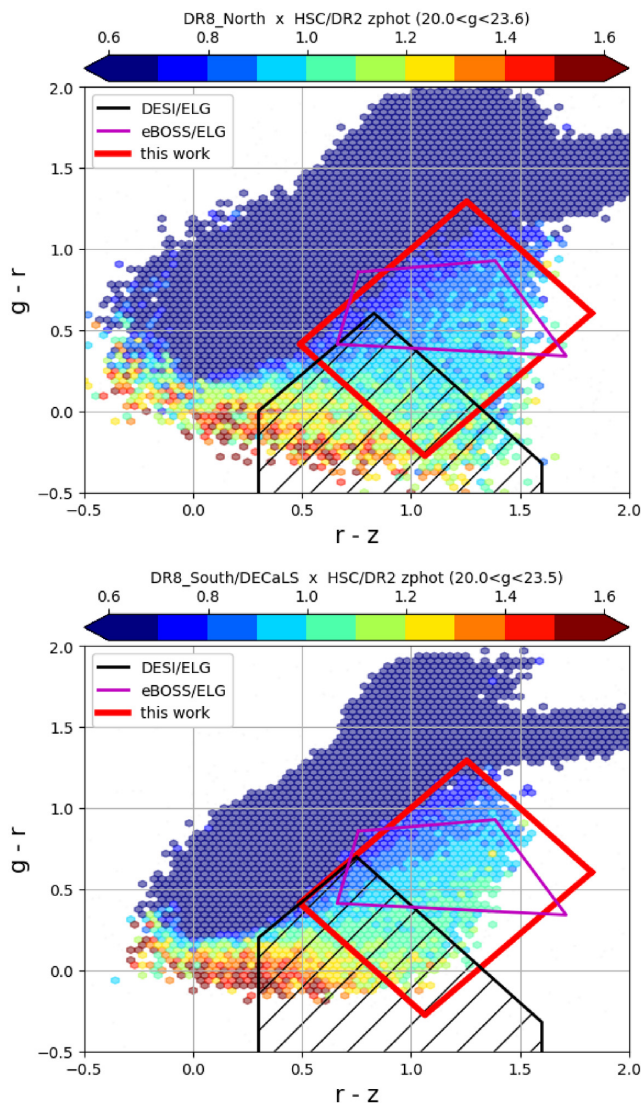[6] https://github.com/moustakas/LSLGA

Figure 5. Colour–colour diagram showing the selection used in this analysis (red), the DESI ELG main selection (black), and the eBOSS ELG selection (magenta). The colour-codding represents photometric redshifts from HSC-PDR2. Top: in BASS/MzLS, bottom: in DECaLS.

areas where higher priority targets prevent any fibre being assigned to a quasar target.

In order to validate our selection, we match our catalogue after applying the colour-cuts and the eBOSS geometry with HSC-PDR2 for the NGC and SGC separately. Fig. 6 shows the resulting redshift distribution for the matched objects in the NGC (blue) and SGC (red) using the HSC-PDR2 photometric redshifts (Nishizawa et al. 2020). The black lines show, respectively, the $n_{\rm p}P_{\rm p} = 1, 3, 5$ surface density when evaluated at wavenumber $k = 0.14\ h$ Mpc^{-1} and orientation relative to the line of sight $\mu = 0.6$. These surface densities assume a fiducial constant bias $b(z)D(z) = 0.84$ from DEEP2 ELG data (Mostek et al. 2013) where $D(z)$ is the linear growth factor normalized by $D(z = 0) = 1$. We can see that the photometric redshift distribution is above $nP = 5$ for $0.6 < z < 1.2$, meaning that in this redshift range we reach a high sampling with an approximate target density of 2900 deg^{-2}. For this reason, we decide to explore the performance of the cross-correlation technique in two redshift ranges: $0.6 \leq z \leq 1.2$ and $0.8 \leq z \leq 1.5$. In the latter, we can expect
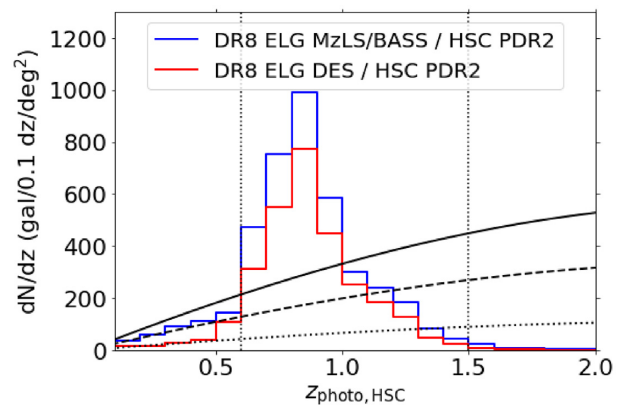
Figure 6. Photometric redshift distribution of the matched galaxies between our photometric sample and HSC PDR2. The blue curve shows the redshift distribution of the matched objects in the BASS/MzLS region and the red curve in the DES region. The dotted, dashed, and solid curves represent, respectively, $n_{\rm p}P_{\rm p} = 1$, $n_{\rm p}P_{\rm p} = 3$, and $n_{\rm p}P_{\rm p} = 5$.

the cross-correlation technique to be less efficient due to a limitation in our capability of selecting a denser sample of galaxies at $z > 1.2$ as we are already pushing the selection to very faint objects ($g_{\rm faint\,end} = 23.5$–23.6), at the limit of detection given the imaging surveys we use ($g_{5\sigma} = 24$).

3.2.2 Imaging systematics and mitigation technique

As for the spectroscopic sample, the number density of ELGs in the photometric sample suffers from observational systematics that arise because of inhomogeneities in the imaging. In order to minimize the impact of these inhomogeneities on our estimate of the true galaxy overdensity field, we apply weights to the photometrically selected galaxies. So far, previous studies using the large-scale structure catalogues such as for BOSS DR12 galaxies (Reid et al. 2016) and for eBOSS DR16 tracers (Ross et al. 2020), were based on multivariate regression techniques to model the dependence between the imaging systematics and the observed target density by usually assuming a linear or quadratic relation. However, for strong contamination like the one close to the Galactic plane, this assumption may be no longer valid. Moreover, the correlations between the Legacy Survey imaging bands are more complex than the ones in SDSS and may not be fully captured by a linear model. Because we are selecting very faint objects at the limit of the survey depth, we also expect the ELG selection to be prone to more fluctuations. For all these reasons, recent progress has been made to develop more advanced systematics mitigation technique, such as the one in Rezaie et al. (2019) based on artificial neural networks (NNs) that has been applied to the DECaLS DR7 data with the eBOSS ELG selection. The approach implements a five-fold partitioning of the data that allows permutation of training, validation, and testing over the entire footprint thereby without a need for multiple realizations of the sky. The methodology presents a multilayer NN with non-linear activation function on the hidden layers that provides a non-linear mapping between the input imaging maps and observed density of ELGs. The network parameters are trained using gradient descent with batches of pixels and minimizing the sum of the residual squared error between the observed density of ELGs and the output of the network, plus an additional L2 regularization term (i.e. proportional to the sum of parameters squared) to suppress overfitting. The hyperparameters include the number of hidden layers, regularization scale, and batch

size that are tuned by applying the trained network on the validation set. Ultimately, the network with the best set of hyper-parameters is applied to the test set. Assuming there is no correlation between the cosmological signal and input imaging maps, the output of the regression, called the *selection mask*, represents solely the systematic effects in the observed density and therefore its inverse can be applied as a weight to galaxies to mitigate the imaging systematics. Rezaie et al. (2019) illustrated that the non-linear NN regression reduces the excess clustering on the largest scales more effectively than the conventional, linear regression.

We apply this technique to the photometric sample used in this analysis and for comparison, we also derive weights based on the standard multivariate linear regression assuming both linear and quadratic terms. In what follows, we summarize the main steps to derive weights based on the NN and a detailed description of the methodology can be found in Rezaie et al. (2019):

(i) We first produce a HEALPIX map (Górski et al. 2005) by splitting the sky into equal-area pixels for the imaging attributes that we consider as potential sources of systematics based on the DR8 ccds-annotated file,[7] using the VALIDATIONTESTS pipeline[8], a modified implementation of QUICKSIP[9] (Leistedt et al. 2015). These maps have a resolution of 13.7 arcmin ($nside = 256$) and we use the following imaging quantities: Galactic extinction (Schlegel et al. 1998), stellar density (Gaia Collaboration 2018), and hydrogen atom column density (Bekhti et al. 2016), as well as galaxy depth, sky brightness, seeing, airmass, exposure time, and Modified Julian Date in r, g, and z pass bands. In total, we have 21 CCD-based maps.

(ii) We use the same modelling and setting parameters for the NN, i.e. the number of hidden layers, type of non-linear activation function and numbers of neurons in each layer as in Rezaie et al. (2019). We also use five folds to train the parameters, tune the hyper-parameters and to estimate the performance of the method. The NN takes as input the imaging attributes as independent variables and the galaxy density as target variable, then it provides as output an estimate of the selection mask (or contamination model) whose inverse corresponds to the photometric weights we can apply to the data.

To estimate the linear correlation between each pair of the imaging attributes and the galaxy density, we compute the Pearson correlation coefficient (PCC) defined by

$$r_{x,y} = \frac{C_{x,y}}{\sqrt{C_{xx}C_{yy}}}, \qquad (11)$$

where $C(x, y)$ corresponds to the covariance between x and y across all pixels. Fig. 7 shows the colour-coded Pearson correlation matrix between each pair of the imaging attributes and the galaxy density (ngal/nran) where the top panel corresponds to DECaLS-North, the middle panel to DECaLS-South, and the bottom panel to BASS/MzLS. First, we confirm that we cannot neglect the correlations between the imaging quantities and the complex shape of the overall matrix needs to be taken into account when correcting for the variations of the galaxy density with these systematics. We can also see different behaviours across the imaging surveys. For instance, as in Rezaie et al. (2019), we also find an anticorrelation between the Galactic foregrounds (stellar density, neutral hydrogen column density, and Galactic extinction) and the observed galaxy density
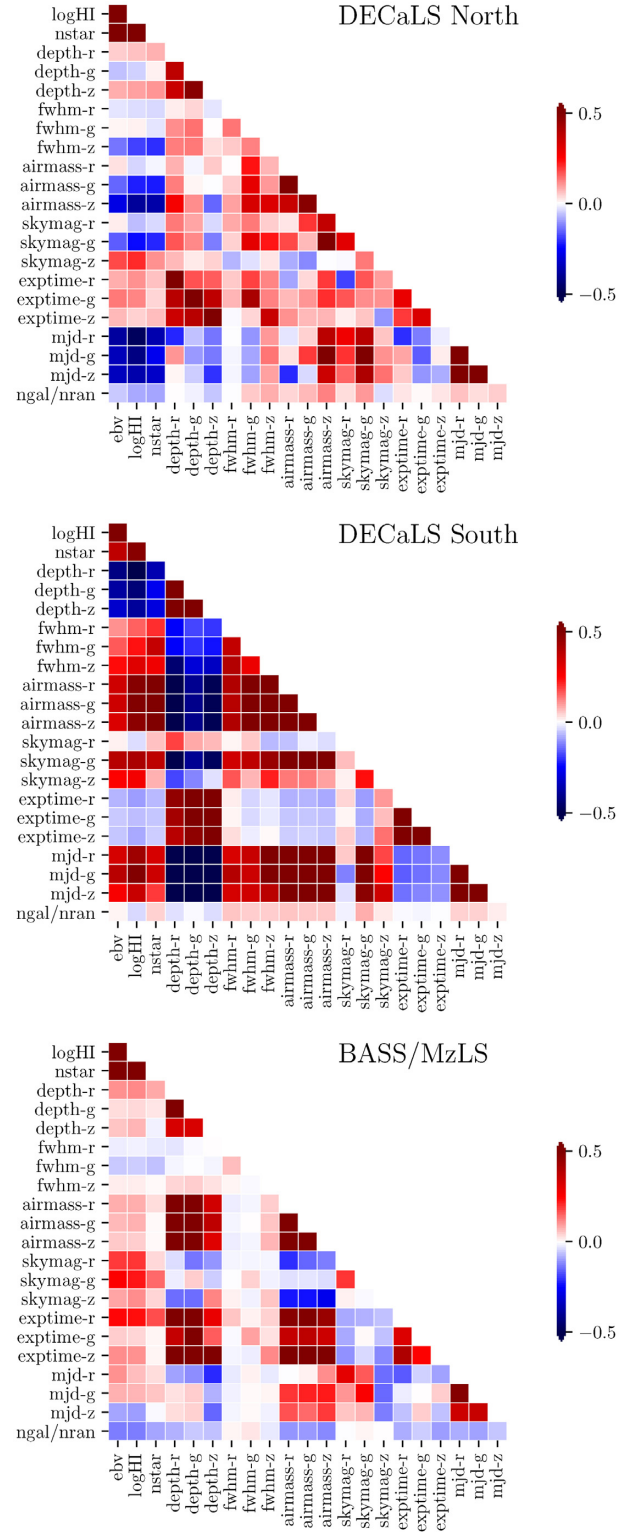

Figure 7. Correlation coefficients between each imaging systematics and the observed galaxy density. Top: DECaLS-North, middle: DECaLS-South, and bottom: BASS/MzLS.

in the NGC with BASS/MzLS and DECaLS-North but we find a positive correlation in DECaLS-South. As expected, the observed galaxy density is also anticorrelated with the depth, because we select more low-z objects with shallower imaging, but the amplitude of the correlation in each band can vary between the surveys.

Because of the different behaviours, the weights are derived by fitting the entire DESI footprint split into BASS/MzLS, DECaLS-North, and DECaLS-South. Fig. 8 shows the target density variations with the most important imaging systematics, where the top panel displays the variation in DECaLS-North, the middle panel in DECaLS-South, and the bottom panel in BASS/MzLS. In all cases, the solid black curve corresponds to the galaxy density without any correction; the dotted curve is using a multivariate regression technique assuming a linear relation between the observed galaxy density and the systematics; the dashed curve assumes a quadratic relation and the solid red line corresponds to the case after applying the NN. As seen with the PCC, for the same systematic quantity we can have different trends of the observed galaxy target density in each region. However, in the three regions, only the NN approach enables correction for the non-linear variations with systematics and recovery of a constant target density. In Section 5.1.2, we will show the impact of each set of weights on the projected cross-correlation function. Another step called 'feature selection' was also added in Rezaie et al. (2019) in order to reduce redundancy among the imaging attributes and to avoid overfitting the cosmological signal. We also apply this step and derive another set of NN weights after applying the feature selection that corresponds to the blue curve in Fig. 8. In our case, it has a marginal impact on the target density variation, the projected cross-correlation function, and the BAO constraints. More details can be found in Appendix A.

In what follows, in order to avoid mixing the surveys and because the analysis is limited to the eBOSS footprint, we remove the region at Dec <32.275 deg[10] in both the spectroscopic and photometric samples to consider BASS–MzLS only in the NGC. We also remove the DES region in the SGC (Dec <5 deg) as it is deeper than DECaLS. Given that we restrict to the eBOSS footprint, the removed regions have small areas so the statistical precision is only slightly affected but in Appendix B, we show that mixing these surveys degrades the cosmological signal significantly.

4 METHODOLOGY

4.1 Clustering estimators

Given that random catalogues are made available for both spectroscopic and photometric objects, we can use the Landy–Szalay estimator (Landy & Szalay 1993):

$$w_\theta(\mathbf{R}) = \frac{D_1 D_2(\mathbf{R}) - D_1 R_2(\mathbf{R}) - D_2 R_1(\mathbf{R}) + R_1 R_2(\mathbf{R})}{R_1 R_2(\mathbf{R})}, \quad (12)$$

where DD, DR, and RR are the paircounts between data–data, data–random, and random–random, respectively, at average separation R. For the spectroscopic data set, we generate a catalogue of randoms 25 times larger than the eBOSS quasar catalogue following the same methodology as in Ross et al. (2020) for the official eBOSS DR16 quasar analysis. For the photometric data set, we take the randoms made for the Legacy Surveys[11] and given the already high-density

sampling, we generate a catalogue of randoms only five times larger than the target catalogue.

We modify the publicly available code TWOPCF[12] to include the calculation of the cross-correlation function binned in transverse comoving separation.

4.2 Covariance matrix

The code can also calculate jackknife errors in a single loop over the galaxy pairs that makes this calculation very efficient. Therefore, we use the jackknife method to estimate our covariance matrix (for a review on the error estimation methods, see Norberg et al. 2009). The covariance matrix is given by

$$C_{i,j} = \frac{N_j - 1}{N_j} \sum_{n=1}^{N_j} [\xi_{l,n}(s_i) - \bar{\xi}_l(s_i)] [\xi_{l',n}(s_j) - \bar{\xi}_{l'}(s_j)], \quad (13)$$

where N_j is the number of jackknife realizations. We divide the footprint into 100 independent sub-regions for both the spectroscopic and photometric sample as showed in Fig. 9. To do so, we create regions of similar area by splitting the survey with straight line cuts in RA and then Dec such that each region contains the same number of points in the random catalogue.

We then compute the corresponding covariance matrix for the monopole of the eBOSS quasars autocorrelation function and the projected cross-correlation function separately after applying their respective weights. For the autocorrelation function, in the redshift range $0.8 \leq z \leq 1.5$, we can compare the covariance matrix and diagonal elements obtained from the 100 jackknife regions and the 1000 eBOSS QSO EZ mocks (Zhao et al. 2020) that are used in the cosmological analysis of the eBOSS DR16 quasars (Neveux et al. 2020; Hou et al. 2021). These mocks are based on the Effective Zel'dovich approximation following the method developed in Chuang et al. (2015); they use seven simulation snapshots to create a lightcone and they are tuned to match the clustering of the final DR16 quasar catalogues. Fig. 10 displays the correlation matrix for the monopole of the autocorrelation function of eBOSS quasars in $0.8 \leq z \leq 1.5$ obtained from the 100 jackknife realizations (left-hand panel) and the 1000 EZ mocks (right-hand panel). The top (respectively bottom) row shows the results for the NGC (respectively SGC). As expected, the correlation matrix from the jackknife method is noisier as it is limited by the number of independent realizations we can create from the survey. We can also compare the diagonal elements as shown in Fig. 11 where we can see the monopole of the autocorrelation function for the NGC (top) and the SGC (bottom) obtained from both methods. They give very similar errors on the measurement while they rely on different assumptions, which gives confidence that both techniques provide a reasonable estimate of the error bar. We also checked that the covariance matrix was stable when varying the number or locations of the jackknife regions.

The correlation matrix of the projected cross-correlation function in the NGC/BASS–MzLS (top panel) and the SGC/DECaLs (bottom panel) is shown in Fig. 12. In this case, we do not have available mocks with the properties of both the photometric and spectroscopic samples so we can only use the jackknife method to fit the data. We checked that the correlation matrix was robust with respect to binning and systematics weights for the photometric sample and in Section 5.2, we will also show the BAO results when fitting each individual jackknife region and taking the mean.

---

[10]https://github.com/desihub/desitarget/blob/master/py/desitarget/io.py#L95

[11]http://www.legacysurvey.org/dr8/files/random-catalogs

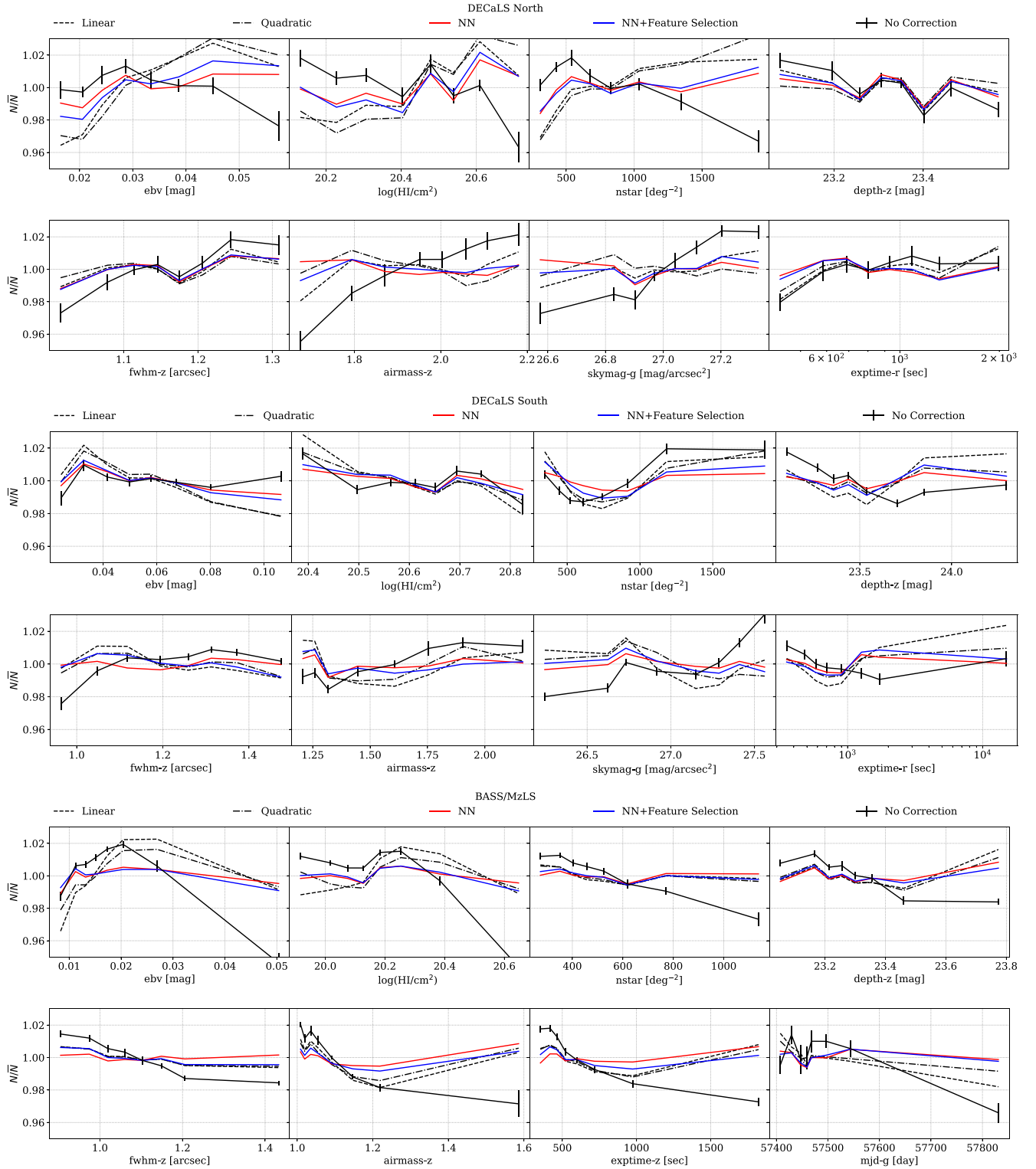[12]https://github.com/lstothert/two_pcf

Figure 8. Target density variation of the photometric sample with imaging systematics before applying weights (black) and after assuming a linear (dotted), quadratic (dashed) or NN based (red) relation between the observed galaxy density and the potential systematics. The blue curves show the correction based on NN and after applying a feature selection that avoids overfitting and is described in Appendix A. Top: DECaLS-North, middle: DECaLS-South, and bottom: BASS/MzLS.
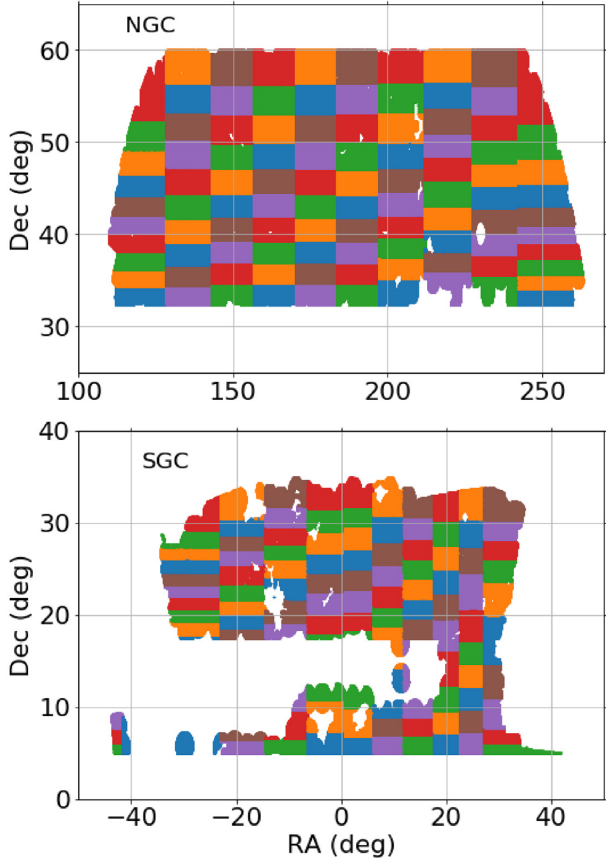
Figure 9. Footprint of the NGC (top panel) and SGC (bottom panel), where colours indicate the 100 jackknife regions.

Figure 11. Monopole of the autocorrelation of eBOSS DR16 quasars in the NGC (top) and SGC (bottom) with error bars coming from the 100 jackknife realizations and from the 1000 EZ mocks.

Figure 10. Correlation matrix obtained from the 100 jackknife regions and used to fit the monopole of the eBOSS quasars autocorrelation function in 25 bins of width 8 h^{-1} Mpc between 0 and 200 h^{-1} Mpc and in the redshift range $0.8 \leq z \leq 1.5$.
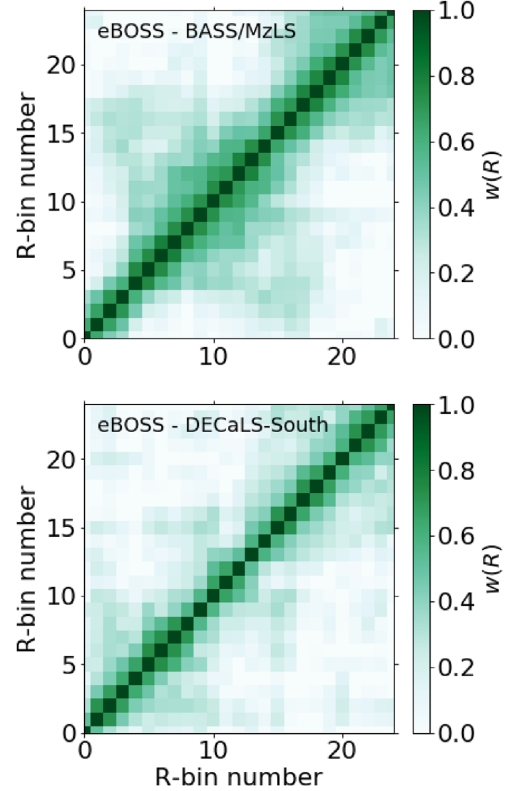
Figure 12. Correlation matrix obtained from the 100 jackknife regions and used to fit the projected cross-correlation in 25 bins of width 8 h^{-1} Mpc between 0 and 200 h^{-1} Mpc.

4.3 BAO fitting procedure

We use a similar BAO fitting procedure for the autocorrelation function of the eBOSS DR16 quasars and the projected cross-correlation function, except for the template. We follow the same methodology as for the BAO analysis in the DR14 eBOSS quasars (Ata et al. 2018) and in the BOSS DR10/DR111 LRG sample (Anderson et al. 2014) and DR9 LRG sample (Anderson et al. 2012).

(i) Compute the two-point statistics (using the LS estimator for the correlation function as described in Section 4.1).

(ii) Generate a template BAO feature (ξ_{temp} or w_{temp}) using the linear power spectrum $P_{\text{lin}}(k)$ obtained from CAMB assuming a fiducial cosmological model.

(iii) Generate a template without the BAO feature where $P_{\text{nw}}(k)$ ('nw' stands for 'no wiggle' that corresponds to no BAO feature in k-space) obtained from the fitting formulae in Eisenstein & Hu (1998) using the same fiducial cosmological model.

We can then model the autocorrelation function following Xu et al. (2012):

$$\xi^{\text{mod}}(s) = B_0 \, \xi_{\text{temp}}(\alpha, s) + A_1 + A_2/s + A_3/s^2, \tag{14}$$

where B_0 is a multiplicative constant allowing for an unknown large-scale bias and $A_{1,2,3}$ are the coefficients of the additive polynomial function to make the results insensitive to shifts in the broad-band shape of the measured correlation function. As in Ata et al. (2018), we apply a Gaussian prior of width 0.4 around the B_0 value found when fitting the template to the data in $10 < s, R < 80 \ h^{-1}$ Mpc without including the broad-band terms.

The BAO template for the correlation function is obtained by Fourier transformation of the power spectrum:

$$\xi_{\text{temp}}(s) = \int \frac{k^2 \mathrm{d}k}{2\pi^2} P_{\text{temp}}(k) j_0(ks) \mathrm{e}^{-k^2 a^2}, \tag{15}$$

where the exponential term has been introduced to damp oscillatory patterns associated with the Bessel function j_0 at high-k and induce better numerical convergence (Anderson et al. 2014). The exact damping scale is not important, in this analysis it is set to $a = 1 \ h^{-1}$ Mpc.

The template for the power spectrum is given by

$$P_{\text{temp}}(k) = P_{\text{nw}}(k) \left[1 + \left(\frac{P_{\text{lin}}(k)}{P_{\text{nw}}(k)} - 1 \right) \mathrm{e}^{-\frac{1}{2} k^2 \Sigma_{\text{nl}}^2} \right], \tag{16}$$

where the BAO signature in linear theory is described by the oscillatory pattern in the $O_{\text{lin}}(k) = P_{\text{lin}}(k)/P_{\text{nw}}(k)$ and the Σ_{nl}^2 term is used to damp the acoustic oscillations in the linear theory power spectrum to account for the effects of non-linear evolution of the density field. As in Ata et al. (2018), we use $\Sigma_{\text{nl}}^2 = 6 \ [h^{-1}\text{Mpc}]^2$ but previous studies showed that the results are insensitive to this choice, as also confirmed in galaxy samples.

For the cross-correlation function template, we use equation (9) with both the linear $P_{\text{lin}}(k)$ and $P_{\text{temp}}(k)$ with the damping term to account for non-linear effects.

For both clustering statistics, we determine how different the BAO scale is in the clustering measurements compared to its location in a template generated using our fiducial cosmology. The observed BAO position can differ from the one in the template because of two main effects. The first effect is related to the fact we do not know the BAO position in the true intrinsic primordial power spectrum, therefore to account for this in the template we include a multiplicative shift that depends on the ratio $r_{\text{drag}}/r_{\text{drag}}^{\text{fid}}$, where r_{drag} is the sound horizon at the drag epoch and corresponds to the expected location of the

BAO feature in comoving distance units. The second effect is due to the fact we need to assume a fiducial cosmological model to convert angles and redshift from the catalogue into comoving coordinates. If the true cosmology is different than the one we assumed, the inferred clustering will contain detectable distortions, in addition to the redshift space distortions due to peculiar velocities. This effect is known as the Alcock–Paczynski effect (Alcock & Paczynski 1979). By introducing two shift parameters, $\alpha_{\parallel}$ and $\alpha_{\perp}$, we can account for this dilation of scales in the direction along and perpendicular to the line of sight. The parameters $\alpha_{\parallel}$ and $\alpha_{\perp}$ can be related to the expansion rate $H(z)$ and the comoving angular diameter distance D_{M} through:

$$\alpha_{\parallel} = \frac{H^{\text{fid}}(z) r_{\text{drag}}^{\text{fid}}}{H(z) r_{\text{drag}}}, \qquad \alpha_{\perp} = \frac{D_{\text{M}}(z) r_{\text{drag}}^{\text{fid}}}{D_{\text{M}}^{\text{fid}}(z) r_{\text{drag}}}. \tag{17}$$

However, given the low statistical precision of the quasar sample in the redshift ranges we consider, it is more optimal to fit an isotropic shift α_{iso} and constrain the spherically averaged distance D_{V} as in Ata et al. (2018):

$$D_{\text{V}} = \left[(1 + z)^2 cz \frac{D_{\text{M}}^2}{H} \right]^{\frac{1}{3}}, \tag{18}$$

where c is the speed of light and α_{iso} is thus defined by

$$\alpha_{\text{iso}} = \frac{D_{\text{V}}(z) r_{\text{drag}}^{\text{fid}}}{D_{\text{V}}^{\text{fid}}(z) r_{\text{drag}}}. \tag{19}$$

Therefore, the autocorrelation function measurements will enable the constraint of $D_{\text{V}}(z)$ by fitting an isotropic shift α_{iso} while the projected cross-correlation function will put constraints on the comoving angular diameter distance $D_{\text{M}}(z)$ by fitting a transverse shift $\alpha_{\perp}$.

4.4 Effective redshift

It is common in standard clustering analyses to approximate the effects of fiducial cosmology as a single rescaling of the cosmological parameters. The redshift range that the eBOSS quasars span is broad, between $z = 0.8$ and $z = 2.2$ and therefore the redshift evolution is more important. Recent techniques using a redshift-weighting have been developed to account for the redshift evolution of the parameters. In Zhu et al. (2018), they performed a BAO analysis of the eBOSS DR14 QSO sample and the constraint they obtained on the spherically averaged distance D_{v} with and without redshift weighting differs by less than 1 per cent. So we can neglect this effect for this analysis where the redshift range is also smaller and consider a single effective redshift. In order to match the definition used for the clustering analysis of the eBOSS DR16 quasars in $0.8 \leq z \leq 2.2$ (Neveux et al. 2020; Hou et al. 2021), we define the effective redshift by

$$z_{\text{eff}} = \frac{\sum_{i,j} w_{\text{tot},i} w_{\text{tot},j} (z_{g,i} + z_{g,j})/2}{\sum_{i,j} w_{\text{tot},i} w_{\text{tot},j}}, \tag{20}$$

where the sum is performed over all galaxy pairs between 0 and $200 \ h^{-1}$ Mpc. We use this definition for the autocorrelation function.

For the cross-correlation function, we do not know the redshift distribution for the photometric sample. Nevertheless, we can make different assumptions and study their impact on the definition of the effective redshift and thus on the cross-correlation function. If we assume the redshift distribution of the photometric sample is flat, then the effective redshift depends only on the distribution of the spectroscopic sample such that $z_{\text{eff},1}$ is given by equation (20).

We also consider another definition, $z_{eff,2}$ where we account for the shape of the redshift distribution of the photometric galaxies by weighting the spectroscopic redshift distribution with the signal-to-noise ratio of the cross-correlation signal. To do so, we divide the quasar sample into redshift bins of width $\Delta z = 0.1$. Finally, we also compute the effective redshift by using the HSC-PDR2 photometric redshifts (Nishizawa et al. 2020) when available with bins of width $\Delta z = 0.1$. For the two redshift ranges we consider, we obtain the following:

$$0.6 \leq z \leq 1.2 : z_{eff,1} = 0.95 \, , \ z_{eff,2} = 0.92 \, , \ z_{eff,3} = 0.93$$
$$0.8 \leq z \leq 1.5 : z_{eff,1} = 1.19 \, , \ z_{eff,2} = 1.10 \, , \ z_{eff,3} = 1.19.$$

The three definitions are in good agreement with relatively close values. Moreover, because we measure a distance relative to the fiducial assumption that has been measured and not an absolute distance, there is indeed some systematic uncertainty on how the impact of the effective redshift choice plays out when testing cosmology, but it is minor. Therefore, in Section 5.2.2, we measure the projected BAO scale assuming $z_{eff,1}$ only but we checked that using $z_{eff,2}$ leads to the same results.

4.5 Parameter inference

We extract the results of the fitting of either the monopole of the autocorrelation function or the projected cross-correlation function by minimizing the χ^2 defined by

$$\chi^2 = (\xi^{Data} - \xi^{Model})C^{-1}(\xi^{Data} - \xi^{Model})^T. \tag{21}$$

where ξ^{Data} corresponds to the measurement, ξ^{Model} to the associated theoretical prediction, and C^{-1} is the inverse of the estimated covariance matrix. When using the 1000 eBOSS QSO EZ mocks (Zhao et al. 2020) to obtain a covariance matrix in $0.8 \leq z \leq 1.5$, we include the Hartlap correction (Hartlap, Simon & Schneider 2007) due to finite number of mocks and number of bins in the analysis that can bias the measurements:

$$C^{-1}_{unbiased} = (1 - D)C^{-1}_{mock} \text{ with } D = \frac{N_b + 1}{N_m - 1}, \tag{22}$$

where N_b is the total number of bins in the measurements and $N_m = 1000$ is the number of realizations.

We use the public code BAOfit[13] to perform the BAO fitting for both the auto- and cross-correlation functions (using our template for the fit to the cross-correlation).

5 RESULTS

5.1 Clustering measurements

5.1.1 Autocorrelation function

We measure the monopole of the autocorrelation function of eBOSS DR16 quasars in the NGC-BASS/MzLS and SGC-DECaLS regions separately and for the two redshift ranges we consider. To do so, we follow the methodology in Ata et al. (2018) where we calculate the autocorrelation function $\xi(s, \mu)$ in evenly spaced bins in s from 0 to 200 h^{-1} Mpc with a bin width of 8 h^{-1} Mpc and 0.01 in μ. The multipoles of the autocorrelation function are then determined by:

$$\xi_l(s) = \frac{2l + 1}{2} \sum_{i=1}^{100} 0.01 \, \xi(s, \mu_i) L_l(\mu_i), \tag{23}$$

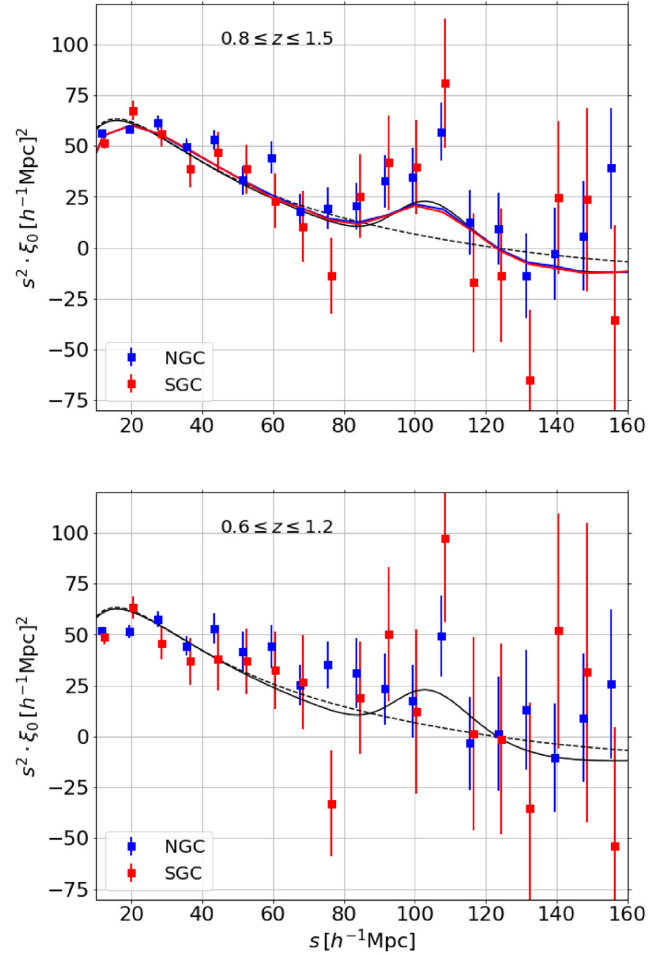[13]https://github.com/ashleyjross/BAOfit

Figure 13. Monopole of the autocorrelation function of the eBOSS DR16 quasars for the NGC (red squares) and SGC (blue squares) for quasars in $0.8 \leq z \leq 1.5$ (top) and $0.6 \leq z \leq 1.2$ (bottom). The solid curves display the mean of the 1000 EZ mocks. The data in each region are consistent with each other and with the mean of the mocks.

where $\mu_i = 0.01i - 0.005$ and L_l is the Legendre polynomial of the order of l. In this work, we use only the monopole ($l = 0$). This definition of the monopole ensures an equal weighting as a function of μ which thus corresponds to a truly spherically averaged observable. Fig. 13 displays the spherically averaged redshift-space autocorrelation function in the NGC (red squares) and SGC (blue squares) for quasars in $0.8 \leq z \leq 1.5$ (top) and $0.6 \leq z \leq 1.2$ (bottom). The solid curves in the top panel show the mean of the 1000 EZ mocks available in this redshift range for the NGC (blue) and SGC (red). The data in each region are consistent with each other, and with the mean of the mocks for the redshift range $0.8 \leq z \leq 1.5$ where EZ mocks are available.

5.1.2 Projected cross-correlation function

As for the autocorrelation function, we compute the projected cross-correlation function in evenly spaced bins in s from 0 to 200 h^{-1} Mpc with a bin width of 8 h^{-1} Mpc. We first investigate the impact of the imaging weights used for the photometric sample on the projected cross-correlation function. As described in Section 3.2, we derived the three sets of weights separately for the two regions, BASS/MzLS and SGC-DECaLS, which together comprise our full DESI footprint.
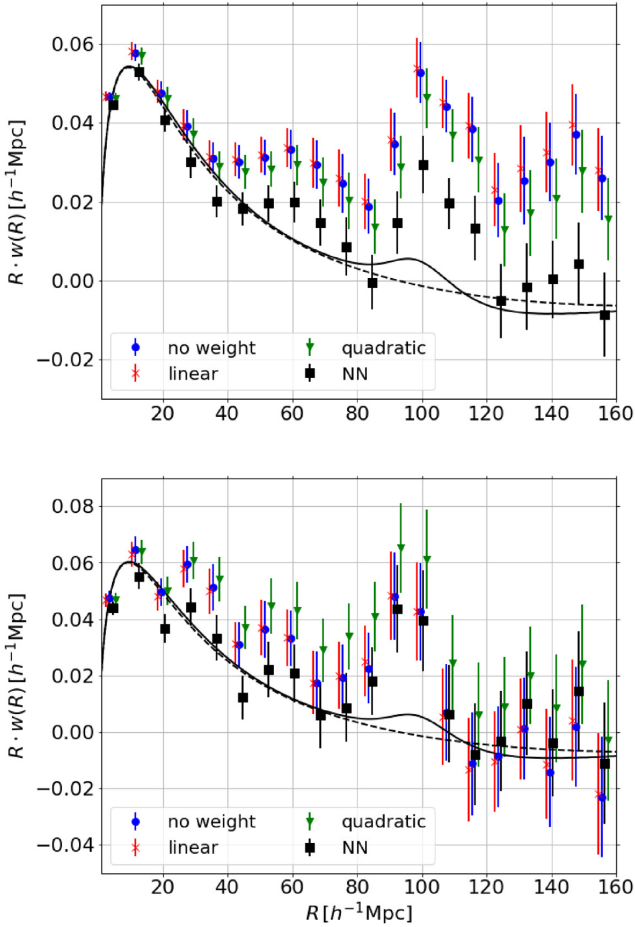
Figure 14. $w(R)$ for NGC-BASS/MzLS (top) and SGC-DECaLS (bottom) regions with and without weights assuming different relations between the observed galaxy density and the potential systematics. The solid (dashed) curve shows the template for the projected correlation function with (without) the BAO feature. For simplicity, we show the redshift range $0.8 \leq z \leq 1.5$ only but we find a similar behaviour for $0.6 \leq z \leq 1.2$.

Each set is based on a different assumption to model the dependence between the observed target density and the imaging attributes: linear relation, quadratic relation, NN.

The projected cross-correlation function in the NGC-BASS/MzLS (top) and SGC-DECaLS (bottom) regions for each type of weights is shown in Fig. 14 for the cross-correlation with quasars in $0.8 \leq z \leq 1.5$. The blue dots correspond to the case without applying imaging weights to the photometric sample, the red dots show the case after applying linear weights, the green dots after applying quadratic weights, and the black dots correspond to the case after applying NN weights. In general, applying the imaging weights improves the agreement with the model (solid black curve with BAO and dashed black curve without) and as expected the weights based on the NN provide the best improvement. However, the agreement is less good around $50 \, h^{-1}$ Mpc (especially in the NGC) and on scales above $\sim 110 \, h^{-1}$ Mpc in the NGC-BASS/MzLS region suggesting that there is some remaining systematics that the NN did not capture and/or which is not contained in the imaging attributes used to train the NN. We found a similar behaviour both for the impact of the different weights and the potential remaining systematics in the NGC when cross-correlating with quasars in $0.6 \leq z \leq 1.2$. We checked that the correlation coefficient between these points is high, typically about

0.75, meaning that the same trend between the points is expected. We also computed the projected correlation function of the quasar sample and the angular correlation function of the photometric sample and nothing unusual was found.

We also note that the amplitude of the BAO feature is more pronounced in the data than in the template. In order to investigate the validity of the template for the projected cross-correlation function given by equation (9), we use the DESI ELG EZ mocks based on the Effective Zel'dovich approximation following the method developed in Chuang et al. (2015). We need to have both the spectroscopic and photometric samples in the same mock realization. Therefore, we use the DESI ELG EZ mocks that have been tuned to match the target density of the main DESI selection which is about 2400 deg^{-2} over the entire DESI footprint and use only the angular coordinates for the photometric sample. In order to mimic the spectroscopic quasar sample, in each mock we consider objects in $0.8 \leq z \leq 1.5$ and randomly downsample them to reach the target density of the eBOSS quasars in this redshift range. By doing so, we do not expect the bias of the samples to be exactly the same as the one of the data, especially for the spectroscopic sample as we know quasars are more biased tracers than ELG. A better way of creating a higher bias sample like the quasar one would be to select the objects based on the background density but the density information is not available in this version of the DESI EZ mocks. We also imprint the inhomogeneities observed in the number density of the ELGs selected from the DESI Legacy Imaging Surveys. The depth of the survey varies across the footprint that introduces a fluctuation in the number of ELGs detected across the sky. This artificial fluctuation is also function of redshift. In order to assess the fluctuation imprinted in the redshift distribution of ELGs, we use a Monte Carlo approach.[14] We take a 3 deg^2 region of DECaLS(DR7) where the photometry is ~ 1.5 magnitude deeper than the average photometry and which is inside the HSC(DR2) footprint (Aihara et al. 2019). We match that sample with the HSC(DR2), and thus have a sample that we consider as our 'truth' sample, where we have deep *grz*-photometry, along with their errors, and a precise redshift estimation from HSC(DR2). We obtain our 'truth' redshift distribution by applying the DESI ELG target selection to that sample. We then imprint the fluctuation in the DESI ELG mocks following these steps:

(i) We divide the DESI footprint in HEALpix pixels and repeat the steps below for each pixel.

(ii) We measure the imaging depth in the three photometric bands g, r, and z.

(iii) We take our 'truth' catalogue and add noise to the photometry according to the depth ratio between the considered HEALpix pixel and the original truth one, and we also account for the Galactic extinction.

(iv) We then apply the DESI ELG target selection on that degraded photometry, and take the ratio of the redshift distribution obtained from that selection to the 'truth' redshift distribution.

(v) We finally take the DESI ELG mock and select all galaxies in the given HEALpix pixel. We then randomly sub-sample the mock galaxies as a function of redshift using the ratio estimated in the previous step.

Fig. 15 shows the difference in standard deviation, σ, between the projected cross-correlation function of the data, w_{data}, and the best-fitting model, w_{temp} given by equation (9), for the redshift range 0.8

---

[14]See this notebook for technical details: https://github.com/desihub/LSS/blob/master/Sandbox/MCeff.ipynb.
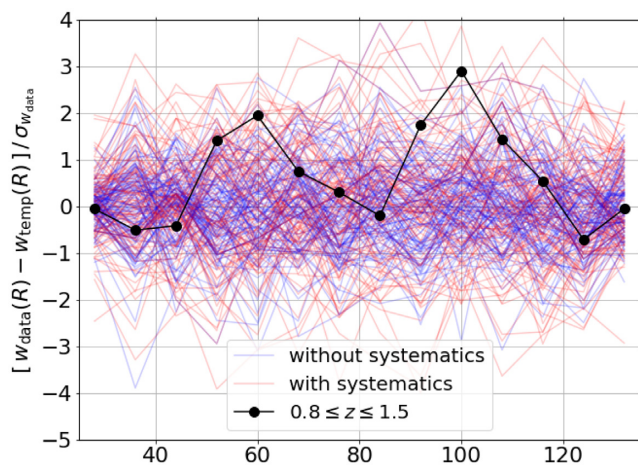
Figure 15. Difference in standard deviation between the projected cross-correlation function of the data and the template given by equation (9). The black dots correspond to the weighted mean of the data, the blue curves show the 100 DESI EZ mocks without imaging systematics, and the red ones with systematics.

$\leq z \leq 1.5$. The black dots show the result for the weighted mean of the data and each blue (red) curve shows one DESI EZ mock without (with) imaging systematics. We can see the 3σ discrepancy at the BAO scale in the data which is counterbalanced by the negative difference in χ^2 from correlations between the offset data point, with other data points. However, the behaviour in the data is not completely unusual when compared to the EZ mocks, suggesting that it could be a statistical fluctuation. We also checked the angular clustering of the photometric galaxies and the standard projected autocorrelation function of the quasars and found nothing unusual either. In Section 5.2.2, we will also present the BAO fits we perform on mocks in order to validate the fitting procedure. When deeper photometric data are available, it would be interesting to look again at this observable. Moreover, when the first set of DESI ELGs spectra are obtained to create a clustering catalogue, it would be worth checking whether the discrepancy at the BAO scale remains.

5.2 BAO measurements

5.2.1 Autocorrelation function

Fig. 16 displays the measurement of the BAO feature in the eBOSS DR16 quasar sample in both redshift ranges: $0.6 \leq z \leq 1.2$ (red) and $0.8 \leq z \leq 1.5$ (blue). In each case, we isolate the BAO feature by subtracting the smooth component of the best-fitting model.

Table 2 summarizes the results of the BAO fits obtained from the autocorrelation of the eBOSS DR16 quasars in the two redshift ranges we consider for our fiducial configuration and the consistency tests we perform on the data. The fiducial configuration uses a bin width of $8 \, h^{-1}$ Mpc, a fitting range $20 < s < 140 \, h^{-1}$ Mpc, a covariance matrix from 100 jackknife realizations and a total weight defined by equation (10) that is applied to both the data and random catalogues. We note that as shown in the BAO analysis of the eBOSS DR14 quasar sample, for instance Ata et al. (2018), at the precision we are working we do not lose constraining power with bins of this width. We note that the difference in the quoted error between the two redshift ranges is large, which could suggest that the BAO fitting response is sensitive to weak BAO peaks due to low statistics. A similar behaviour was found with the eBOSS DR14 quasar sample when splitting the redshift sample into 2 redshift bins,
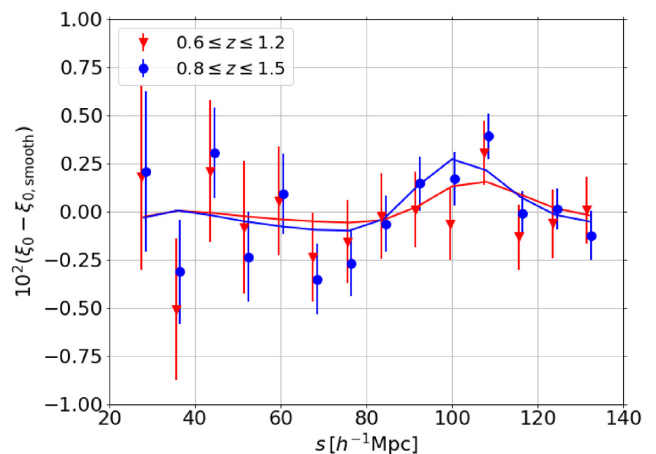
Figure 16. The spherically averaged BAO signal of the eBOSS DR16 quasars in $0.6 \leq z \leq 1.2$ (red) and $0.8 \leq z \leq 1.5$ (blue). The smooth component of the best-fitting model has been substracted to both the best-fitting model and the measurements in order to isolate the BAO feature.

Table 2. Results for the isotropic BAO fits to the autocorrelation of the DR16 eBOSS quasars. The fiducial configurations use data with $8 \, h^{-1}$ Mpc bin size and centres in the range $20 < s < 140 \, h^{-1}$ Mpc and a covariance matrix from 100 jackknife realizations.

Configuration	$\alpha_{\rm iso}$	χ^2/d.o.f.
$0.8 \leq z \leq 1.5$		
Fiducial	1.013 ± 0.036	12.5/9
mean of the jackknifes	1.014 ± 0.034	13.3/9
$\Delta s = 5 \, h^{-1}$ Mpc	1.036 ± 0.035	23.4/19
EZmock cov fiducial	1.005 ± 0.033	14.5/9
EZmock cov $5 \, h^{-1}$ Mpc	1.003 ± 0.034	24.8/19
$20 < s < 150 \, h^{-1}$ Mpc	1.031 ± 0.036	14.7/11
$10 < s < 140 \, h^{-1}$ Mpc	1.029 ± 0.035	15.1/11
no $w_{\rm sys}$	1.017 ± 0.035	12.4/9
NGC	1.009 ± 0.044	9.7/9
SGC	1.044 ± 0.063	11.0/9
$0.6 \leq z \leq 1.2$		
Fiducial	1.003 ± 0.096	6.0/9
mean of the jackknifes	0.999 ± 0.092	6.4/9
$\Delta s = 5 \, h^{-1}$ Mpc	1.019 ± 0.096	18.4/19
$20 < s < 150 \, h^{-1}$ Mpc	1.037 ± 0.106	7.0/11
$10 < s < 140 \, h^{-1}$ Mpc	1.016 ± 0.090	6.2/11
no $w_{\rm sys}$	0.990 ± 0.090	6.2/9
NGC	1.008 ± 0.098	5.3/9
SGC	1.003 ± 0.101	7.6/9

although the difference in the volume probed by each redshift bin was also bigger (Gil-Marín et al. 2018). We also fit the individual jackknife realizations and report the mean result for the value and the error bar. As expected, both the full sample and the mean of the jackknife regions are consistent with each other. Then, we perform several consistency tests by varying the binning, the fitting range and for $0.8 \leq z \leq 1.5$, we also look at the impact of changing the covariance matrix by using the one from the eBOSS QSO mocks. All the results are consistent with each other within 1σ, demonstrating the robustness of the BAO feature in the spherically averaged autocorrelation function.
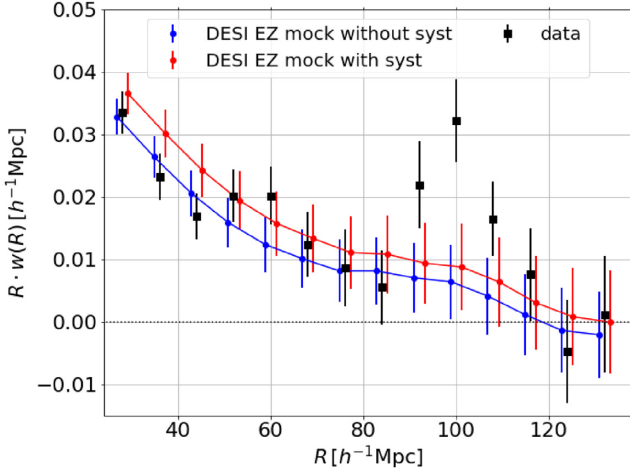
Figure 17. Projected cross-correlation function for the weighted mean of the data (black) compared to the mean of the 100 DESI EZ mocks without (blue) and with (red) imaging systematics. For each EZ mock, the error bar is obtained using 100 jackknife realizations and we show the mean of the error bars for the 100 DESI EZ mocks. For this test, we use quasars in $0.8 \leq z \leq 1.5$.

5.2.2 Projected cross-correlation function

In order to validate the BAO fitting procedure using the projected cross-correlation function, we first apply the pipeline on the DESI EZ mocks. Fig. 17 displays the projected cross-correlation function of the weighted mean of the data (NGC with BASS/MzLS and SGC with DECaLS-S) in black dots with error bars corresponding to the diagonal elements of the covariance matrix obtained from the 100 jackknife realizations. We also show the mean of the DESI EZ mocks without (blue dots) and with (red dots) systematics while the solid curves show the best-fitting model in each case. In both cases, the error bar corresponds to the mean of the error bars from the 100 DESI EZ mocks. For each EZ mock, the error bar is obtained using 100 jackknife realizations such that the fit to each DESI EZ mock is under the same fitting conditions as for the data. Given that the DESI mocks do not completely represent both the photometric and spectroscopic samples by construction, we prefer not to use them to determine the uncertainties on the measurements from the data. We can see that the amplitude of the BAO signal in the mocks is consistent with the template, which confirms the validity of the template. Adding imaging systematics to the mocks yields a constant offset in the projected cross-correlation function but which can be taken into account in the best-fitting model with the normalization factor.

The results of the BAO fitting are shown in Fig. 18 where the top panel displays the value and error obtained on the BAO position for each mock without (blue) and with (red) systematics, compared to the result for the data (black star). We fit the individual DESI EZ mocks with their covariance matrix from $20 < s < 140\ h^{-1}$ Mpc. Only mocks with a 'BAO detection' are kept meaning that they have $\Delta \chi^2 \geq 1$ within $0.8 < \alpha < 1.2$. Over 75 per cent (70 per cent) of the DESI EZ mocks without (with) imaging systematics satisfy this condition. The bottom panel shows the χ^2 distribution of the mocks compared to the value for the data. The BAO measurement in the data is consistent with the statistics of the mocks, both in terms of BAO position and χ^2, which therefore validates the fitting procedure for the projected cross-correlation function. We also check that the BAO results are robust when using the damping term Σ_{NL} that accounts
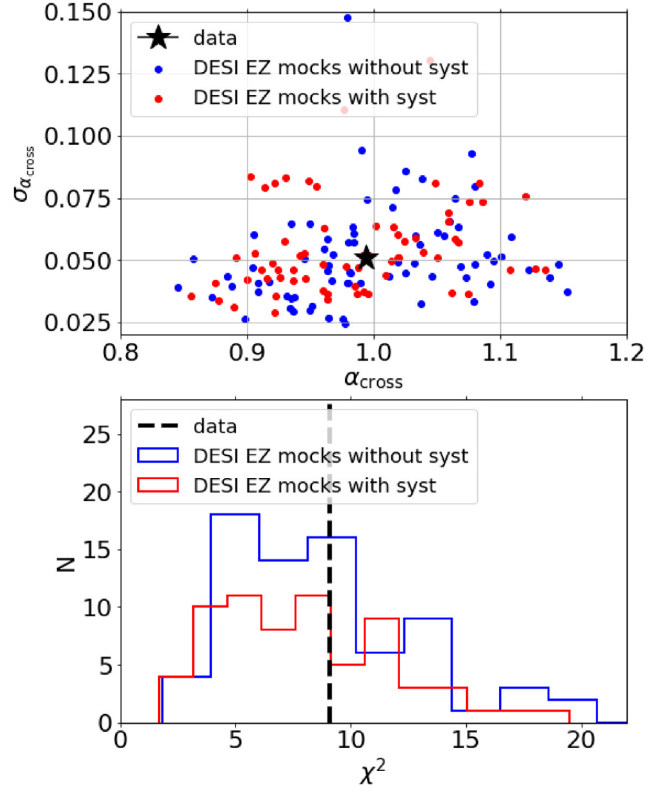
Figure 18. Results of the BAO fitting of the DESI EZ mocks in $0.8 \leq z \leq 1.5$. Top: Value and error bar of α_{cross} for each individual mock without (blue) and with (red) imaging systematics from the Legacy Imaging Surveys. The black star shows the result of the data. Bottom: Distribution of the χ^2 for the mocks without (blue) and with (red) imaging systematics compared to the χ^2 of the data in dashed black.

for non-linear effects in the BAO template as in the autocorrelation function. We report the mean value of the 100 individual EZ mocks on the projected BAO parameter α_{cross}: Without systematics

$$\Sigma_{NL}^2 = 0\ [h^{-1}\ \mathrm{Mpc}]^2 : \alpha_{cross} = 0.998 \pm 0.051$$
$$\Sigma_{NL}^2 = 6\ [h^{-1}\ \mathrm{Mpc}]^2 : \alpha_{cross} = 1.001 \pm 0.058.$$

With systematics

$$\Sigma_{NL}^2 = 0\ [h^{-1}\ \mathrm{Mpc}]^2 : \alpha_{cross} = 0.985 \pm 0.057$$
$$\Sigma_{NL}^2 = 6\ [h^{-1}\ \mathrm{Mpc}]^2 : \alpha_{cross} = 0.982 \pm 0.058.$$

Fig. 19 displays the BAO measurements for the weighted mean of the projected cross-correlation function when using quasars in $0.6 \leq z \leq 1.2$ (red) and $0.8 \leq z \leq 1.5$ (blue) together with the best-fitting model in solid curves for our fiducial configuration: bin width of 8 h^{-1} Mpc, fitting range $20 < s < 140\ h^{-1}$ Mpc and a covariance matrix from 100 jackknife realizations. We can see that the amplitude of the cross-correlation signal is higher for the redshift range $0.6 \leq z \leq 1.2$, meaning that more photometric ELGs lie in this redshift range as expected according to the photometric redshift distribution shown in Fig. 6.

Table 3 summarizes the results of the BAO fits obtained from the projected cross-correlation in the two redshift ranges we consider for our fiducial configuration with a bin width of 8 h^{-1} Mpc, a fitting range $20 < s < 140\ h^{-1}$ Mpc, a covariance matrix from 100 jackknife realizations. Despite the apparent bad fits, the χ^2 are fine and we remind that the data points are very correlated with each other. As for the autocorrelation function, we also fit the individual jackknife
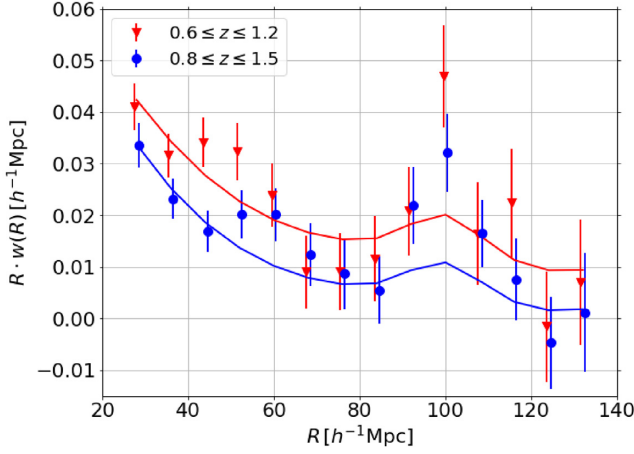
Figure 19. The projected cross-correlation function for $0.6 \le z \le 1.2$ (red) and $0.8 \le z \le 1.5$ (blue) and the acoustic scale region. The solid curves represent the best-fitting model in each case.

Table 3. Results for the projected BAO fits to the cross-correlation of the DR16 eBOSS quasars with ELG galaxies from DESI DR8 Legacy Imaging Surveys. The fiducial configurations use data with 8 h^{-1} Mpc bin size and centres in the range $10 < s < 140$ h^{-1} Mpc and a covariance matrix from 100 jackknife realizations.

Configuration	α_{cross}	χ^2/d.o.f.
$0.8 \le z \le 1.5$		
Fiducial	0.994 ± 0.051	9.1/9
mean of the jackknifes	0.994 ± 0.051	9.3/9
$\Sigma_{\text{NL}} = 6 \, [h^{-1}\,\text{Mpc}]^2$	0.993 ± 0.055	9.4/9
$\Delta s = 5 \, h^{-1}$ Mpc	1.005 ± 0.047	17.3/19
$20 < s < 150 \, h^{-1}$ Mpc	0.997 ± 0.049	9.4/11
$10 < s < 140 \, h^{-1}$ Mpc	0.998 ± 0.052	10.8/11
no w_{sys}	0.995 ± 0.044	8.6/9
$w_{\text{sys-lin}}$	0.989 ± 0.046	7.5/9
$w_{\text{sys-quad}}$	0.988 ± 0.046	8.4/9
$w_{\text{sys-nn} - \text{fs}}$	0.993 ± 0.046	9.4/9
NGC	0.970 ± 0.066	7.8/9
SGC	1.025 ± 0.109	5.9/9
$0.6 \le z \le 1.2$		
Fiducial	0.999 ± 0.059	13.1/9
mean of the jackknifes	0.999 ± 0.059	13.3/9
$\Sigma_{\text{NL}} = 6 \, [h^{-1}\,\text{Mpc}]^2$	0.998 ± 0.063	13.2/9
$\Delta_s = 5 \, h^{-1}$ Mpc	1.014 ± 0.058	20.2/19
$20 < s < 150 \, h^{-1}$ Mpc	0.991 ± 0.059	14.8/11
$10 < s < 140 \, h^{-1}$ Mpc	1.003 ± 0.061	13.5/11
no w_{sys}	1.004 ± 0.057	11.3/9
$w_{\text{sys-lin}}$	0.997 ± 0.059	12.9/9
$w_{\text{sys-quad}}$	0.994 ± 0.058	13.7/9
$w_{\text{sys-nn} - \text{fs}}$	0.999 ± 0.056	13.4/9
NGC	0.965 ± 0.078	16.2/11
SGC	1.045 ± 0.112	5.3/11

realizations and report the mean result for both the value and the error bar. As expected, both the full sample and the mean of the jackknife regions are consistent with each other. Table 3 also shows the results of the consistency tests when including the damping term Σ_{NL} that accounts for non-linear effects, when varying the binning, the fitting range and when using different imaging weights for the photometric sample. We also find very similar results on α_{cross} between the three definitions of the effective redshift described in Section 4.4. All the results are consistent with each other within 1σ, demonstrating
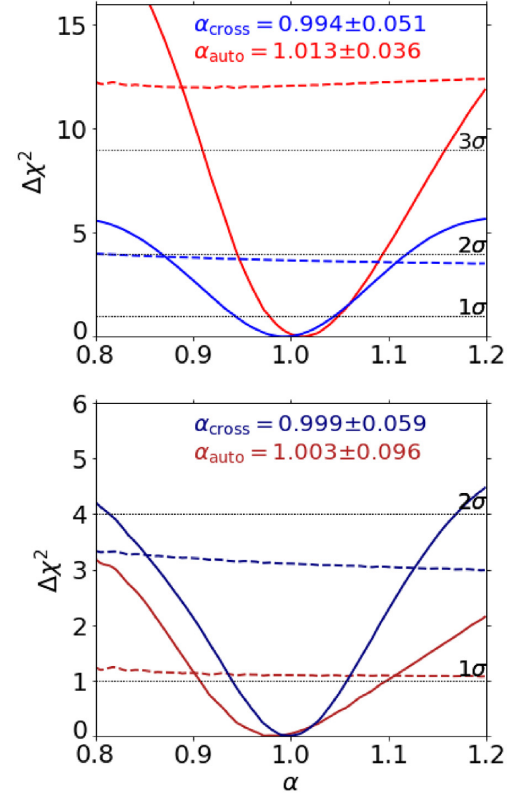
Figure 20. Likelihood of the transverse BAO parameter α_{cross} in terms of $\Delta\chi^2$ in the redshift ranges $0.8 \le z \le 1.5$ (top) and $0.6 \le z \le 1.2$ (bottom). In each panel, the solid curves display the likelihood obtained when fitting the data with a model that contains the BAO feature, while the dashed curves display the same information for a model without BAO.

the robustness of the BAO feature in the projected cross-correlation function.

5.3 BAO constraints and discussion

Fig. 20 displays the likelihood and BAO detection significance in terms of $\Delta\chi^2$ obtained from the auto- and projected cross-correlation function in $0.8 \le z \le 1.5$ (top) and $0.6 \le z \le 1.2$ (bottom). The dashed curves represent the template without the BAO feature in each case. The likelihoods from the autocorrelation function (red and dark red) are more skewed towards large values of α compared to the ones from the projected cross-correlation function. In both redshift ranges, the BAO detection significance is about 2σ for the projected cross-correlation function while it is greater than 3σ in $0.8 \le z \le 1.5$ and less than 1.5σ in $0.8 \le z \le 1.5$ for the autocorrelation function.

In both redshift ranges, the statistics are too low to enable an anisotropic BAO measurement from the autocorrelation function of the eBOSS DR16 quasar sample but Hou et al. (2021) and Neveux et al. (2020) did the anisotropic BAO fitting using eBOSS DR16 quasars in $0.8 \le z \le 2.2$. Both techniques provide consistent results within less than 0.5σ, showing the robustness of the BAO feature in galaxy clustering. However, the BAO shifts are not sensitive to exactly the same cosmic distance as presented in Section 4.5. The BAO shift from the autocorrelation is sensitive to the spherically averaged distance D_V while the BAO shift from the projected cross-correlation function is sensitive to the angular diameter distance D_M

Table 4. Comparison between the autocorrelation and the projected cross-correlation functions for this work (top rows) and Patej & Eisenstein (2018, bottom row) in terms of redshift range, target density, and constraints on the BAO scale.

Redshift range	Area (deg^2)	Spectro (deg^{-2})	Photo (deg^{-2})	σ_{auto}	σ_{cross}
$0.8 \leq z \leq 1.5$	4000	35	2100	3.5 per cent	5 per cent
$0.6 \leq z \leq 1.2$	4000	20	2900	9 per cent	6 per cent
$0.6 < z < 0.8$	6000	35	1100	–	3 per cent

such that we obtain:

$$0.8 \leq z \leq 1.5 \; z_{eff} = 1.20$$
$$\text{auto}: D_V(z_{eff})/r_{drag} = 26.53 \pm 0.94$$
$$\text{cross}: D_M(z_{eff})/r_{drag} = 30.42 \pm 1.56$$
$$0.6 \leq z \leq 1.2 \; z_{eff} = 0.92$$
$$\text{auto}: D_V(z_{eff})/r_{drag} = 26.3 \pm 2.5$$
$$\text{cross}: D_M(z_{eff})/r_{drag} = 30.6 \pm 1.8.$$

In the redshift range $0.6 \leq z \leq 1.2$ where we expect to have more ELGs, we indeed obtain a more precise distance measurement with the projected cross-correlation function than with the autocorrelation function (5.9 per cent against 9.5 per cent). However, as mentioned above, the BAO detection significance remains low in both cases. The comparison between the two redshift ranges suggests that it is essential to ensure the best overlap in redshift between the spectroscopic and photometric samples. Moreover, it seems to suggest that although the spectroscopic target density may be too low to obtain a strong BAO detection in the autocorrelation function, we can expect a stronger detection in the projected cross-correlation function. Table 4 summarizes the configuration for each redshift range with the target density for each sample and the precision on the BAO scale obtained from the auto- and projected cross-correlation function. The first two rows correspond to this work where the galaxy density of the photometric sample in each redshift range is computed using the photometric redshifts of Fig. 6. We also show the configuration in Patej & Eisenstein (2018) in the third row, but the authors did not provide a BAO measurement from the autocorrelation function of their spectroscopic sample; this is why we did not quote a precision for σ_{auto} in $0.6 < z < 0.8$. The number densities in our analysis are more optimal for this type of cross-correlation (mainly a denser photometric sample), so we may have expected a more precise measurement from the projected cross-correlation function but we also have more important systematics in the photometric sample obtained from the DESI Legacy Imaging Surveys as we pushed towards very faint objects to reach a high sampling of galaxies at high redshifts ($z > 1$). Moreover, Patej & Eisenstein (2018) used a narrower redshift bin that could also help improve the constraint from the projected cross-correlation function.

However, the comparison with the autocorrelation function is very encouraging, showing that we can not only detect the BAO feature in the projected cross-correlation function but also put better constraints when the spectroscopic target density is too low to enable a strong BAO detection in the autocorrelation function. We also compare our measurements of D_M with other measurements using different tracers and methods, as shown in Fig. 21: BOSS DR12 LRG results using BAO only (Alam et al. 2017); DES Y1 using photometric data in a combined analysis with weak lensing and clustering (DES Collaboration 2018); the eBOSS final results (eBOSS Collaboration 2020) including eBOSS + BOSS LRG using BAO only (Gil-Marín et al. 2020; Bautista et al. 2021), eBOSS
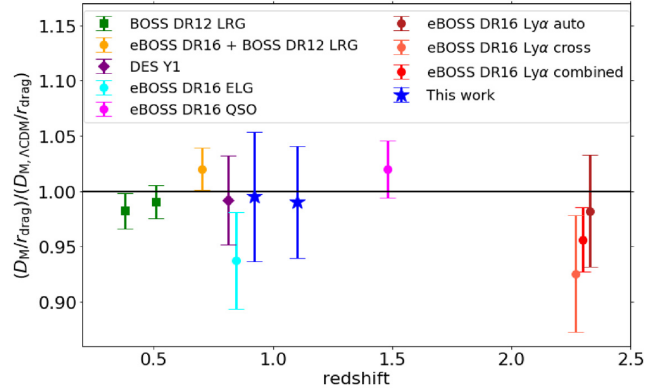
Figure 21. Measurements of the comoving angular diameter distance D_M as a function of redshift. Our measurements at $z_{eff} = 0.92$ and $z_{eff} = 1.1$ are shown using a blue star.

ELG using BAO + RSD[15] (Tamone et al. 2020; de Mattia et al. 2021), eBOSS QSO using BAO only (Neveux et al. 2020; Hou et al. 2021), and eBOSS Lyα forests (du Mas des Bourboux et al. 2020) using BAO from the autocorrelation Lyα/Lyα (dark red), cross-correlation Lyα/quasar (light red), and the combined measurement (red). This latest example shows the gain in precision on the combined measurement from auto- and cross-correlation. Although the analysis in this work is very different from the one of the Lyα forests, in future work it would be interesting to investigate the potential gain on D_M of combining the auto- and projected cross-correlation function.

6 CONCLUSIONS

We have applied a method proposed in Patej & Eisenstein (2018) based on the cross-correlation between a sparse spectroscopic sample and a denser photometric sample to constrain the angular diameter distance by searching for the transverse BAO. We have used a sample of SDSS-IV eBOSS quasars between $0.6 \leq z \leq z1.5$ and we have produced a high-density sample of galaxies using the DESI Legacy Imaging Surveys. Since we need to select fainter objects at the limit of the survey depth, we expect the photometric sample to be more prone to density fluctuations due to inhomogeneities in the selection. To mitigate for this effect, we have applied the NN technique developed in Rezaie et al. (2019) to our photometric sample and confirmed that it can correct for complex variations that standard multivariate linear regression techniques cannot. We have validated the pipeline of the projected cross-correlation function against approximate mocks and we have demonstrated that the BAO measurement with this method is robust against a variety of observational choices.

---

[15]The statistics of the eBOSS ELG sample is not enough to perform an anisotropic BAO fitting and thus to measure D_M from BAO only.

We have performed two analyses in parallel: the autocorrelation of the eBOSS quasars and the projected cross-correlation function in order to provide a detailed comparison. We have investigated two configurations: one where we cross-correlate the photometric galaxies with quasars in $0.8 \leq z \leq 1.5$ and another one with quasars in $0.6 \leq z \leq 1.2$. In the latter, we find that the cross-correlation technique can reduce shot noise and thus provide better constraints on the cosmic distance (6 per cent precision) compared to the results obtained from the autocorrelation (9 per cent precision). However, we also find that we are limited by the number density and purity of the photometric sample and its overlap in redshift with the spectroscopic sample, which thus affects the performance of the method. We also find a noticeable peak in the acoustic scale region that is larger than expected in usual theories, although the fits with templates based on the matter power spectrum yield only a 2σ indication. We compare the amplitude of the signal in the acoustic scale region with approximate mocks and we perform a series of consistency tests that indicate no bias on the cosmological constraint we derive from the fits of the projected cross-correlation function. Nevertheless, we highlight that DESI will soon start its cosmological survey and it would be worth checking whether the discrepancy at the BAO scale remains when the clustering catalogues are available.

In addition, the technique will be even more promising with the arrival of deeper photometric data, thanks to upcoming surveys such as *Euclid* (Amendola et al. 2013). The method could be applied to DESI quasars, which will still be limited by shot noise (DESI Collaboration 2016a), with a sample of H α ($0.7 < z < 2$) and [O III] emission galaxies ($2 < z < 2.7$) selected from *Euclid* (Mehta et al. 2015). This should enable to put better constraints on the transverse BAO scale at $z \geq 2$ than DESI will with the autocorrelation function of the quasars alone.

DATA AVAILABILITY

The photometric data underlying this article are publicly available as part of the DESI Legacy Imaging Surveys at https://www.legacysurvey.org/dr8/description/. The spectroscopic data underlying this article are available to the public at https://data.sdss.org/sas/dr16/eboss/lss/catalogs/DR16/ and are described at https://www.sdss.org/dr16/spectro/lss/.

REFERENCES

Aihara H. et al., 2018, PASJ, 70, S4
Aihara H. et al., 2019, PASJ, 71, 114
Alam S. et al., 2017, MNRAS, 470, 2617
Alcock C., Paczynski B., 1979, Nature, 281, 358
Amendola L. et al., 2013, Living Rev. Relativ., 16, 6
Anderson L. et al., 2012, MNRAS, 427, 3435
Anderson L. et al., 2014, MNRAS, 441, 24
Ata M. et al., 2018, MNRAS, 473, 4773
Bautista J. E. et al., 2021, MNRAS, 500, 736
Bekhti N. B. et al., 2016, A&A, 594, A116
Bovy J. et al., 2012, ApJ, 749, 41
Chuang C.-H., Kitaura F.-S., Prada F., Zhao C., Yepes G., 2015, MNRAS, 446, 2621
Cole S. et al., 2005, MNRAS, 362, 505

Davis M., Peebles P. J. E., 1983, ApJ, 267, 465
Dawson K. S. et al., 2016, AJ, 151, 44
de Jong J. T. A. et al., 2015, A&A, 582, A62
de Mattia A. et al., 2021, MNRAS, 501, 5616
DES Collaboration, 2018, Phys. Rev. D, 98, 043526
DESI Collaboration, 2016a, preprint (arXiv:1611.00036)
DESI Collaboration, 2016b, preprint (arXiv:1611.00037)
Dey A. et al., 2019, AJ, 157, 168
du Mas des Bourboux H. et al., 2020, ApJ, 901, 153
eBOSS Collaboration, 2020, preprint (arXiv:2007.08991)
Eisenstein D. J., Hu W., 1998, ApJ, 496, 605
Eisenstein D. J. et al., 2005, ApJ, 633, 560
Eisenstein D. J., Seo H.-J., White M., 2007, ApJ, 664, 660
Feldman H. A., Kaiser N., Peacock J. A., 1994, ApJ, 426, 23
Freedman W. L. et al., 2019, ApJ, 882, 34
Fukugita M., Ichikawa T., Gunn J. E., Doi M., Shimasaku K., Schneider D.
    P., 1996, AJ, 111, 1748
Gaia Collaboration, 2018, A&A, 616, A1
Gil-Marín H. et al., 2018, MNRAS, 477, 1604
Gil-Marín H. et al., 2020, MNRAS, 498, 2492
Górski K. M., Hivon E., Banday A. J., Wand elt B. D., Hansen F. K., Reinecke
    M., Bartelmann M., 2005, ApJ, 622, 759
Gunn J. E. et al., 2006, AJ, 131, 2332
Guzzo L. et al., 2008, Nature, 451, 541
Hartlap J., Simon P., Schneider P., 2007, A&A, 464, 399
Hou J. et al., 2021, MNRAS, 500, 1201
Kitanidis E. et al., 2020, MNRAS, 496, 2262
Landy S. D., Szalay A. S., 1993, ApJ, 412, 64
Lang D., Hogg D. W., Mykytyn D., 2016, Astrophysics Source Code Library,
    record ascl:1604.008
Leistedt B. et al., 2015, ApJS, 226, 24
Lewis A., Challinor A., Lasenby A., 2000, ApJ, 538, 473
Linder E. V., Cahn R. N., 2007, Astropart. Phys., 28, 481
LSST Dark Energy Science Collaboration, 2012, preprint (arXiv:1211.0310)
Lyke B. W. et al., 2020, ApJS, 250, 8
Madau P., Dickinson M., 2014, ARA&A, 52, 415
Mehta V. et al., 2015, ApJ, 811, 141
Mostek N., Coil A. L., Cooper M., Davis M., Newman J. A., Weiner B. J.,
    2013, ApJ, 767, 89
Myers A. D. et al., 2015, ApJS, 221, 27
Neveux R. et al., 2020, MNRAS, 499, 210
Newman J. A., 2008, ApJ, 684, 88
Nishizawa A. J., Oguri M., Takada M., 2013, MNRAS, 433, 730
Nishizawa A. J., Hsieh B.-C., Tanaka M., Takata T., 2020, preprint
    (arXiv:2003.01511)
Norberg P., Baugh C. M., Gaztañaga E., Croton D. J., 2009, MNRAS, 396,
    19
Padmanabhan N. et al., 2007, MNRAS, 378, 852
Padmanabhan N., White M., Norberg P., Porciani C., 2009, MNRAS, 397,
    1862
Patej A., Eisenstein D. J., 2018, MNRAS, 477, 5090
Planck Collaboration VI, 2020, A&A, 641, A6
Raichoor A. et al., 2017, MNRAS, 471, 3955
Reid B. et al., 2016, MNRAS, 455, 1553
Rezaie M., Seo H.-J., Ross A. J., Bunescu R. C., 2019, MNRAS, 495, 1613
Riess A. G. et al., 2018, ApJ, 861, 126
Riess A. G., Casertano S., Yuan W., Macri L. M., Scolnic D., 2019, ApJ, 876,
    85
Ross A. J. et al., 2011, MNRAS, 417, 1350
Ross A. J., Percival W. J., Manera M., 2015, MNRAS, 451, 1331
Ross A. J. et al., 2020, MNRAS, 498, 2354
Schlafly E. F., Finkbeiner D. P., 2011, ApJ, 737, 103
Schlegel D. J., Finkbeiner D. P., Davis M., 1998, ApJ, 500, 525
Smee S. A. et al., 2013, AJ, 146, 32
Smith R. E. et al., 2003, MNRAS, 341, 1311
Takahashi R., Sato M., Nishimichi T., Taruya A., Oguri M., 2012, ApJ, 761,
    152
Tamone A. et al., 2020, MNRAS, 499, 5527

Wright E. L. et al., 2010, AJ, 140, 1868
Xu X., Padmanabhan N., Eisenstein D. J., Mehta K. T., Cuesta A. J., 2012,
    MNRAS, 427, 2146
Zhao C. et al., 2020, preprint (arXiv:2007.08997)
Zhu F. et al., 2018, MNRAS, 480, 1096

APPENDIX A: NEURAL NETWORK WITH FEATURE SELECTION

Because the imaging attributes are correlated, they can contain redundant information which increases the risk of overfitting and degrading the cosmological clustering. Within the NN framework, we can apply a feature selection process to identify the redundant and irrelevant imaging maps (and thus reduce the number of input imaging attributes) by splitting the data into five partitions. We train a linear model on all the input imaging quantities and then eliminate one and train again the model on the remaining input features. Note that given the definition of the minimization function, if the feature contains relevant information on the systematic effect, it would make the fit worse and the model would yield a higher validation error. This procedure removes one map at a time iteratively, and finally it ranks the imaging maps such that the features which produce the highest improvement in fitting are removed. Fig. A1 shows the results of the feature selection procedure described above where the darker the dot, the more important the imaging attribute, for DECaLS-South (left) and BASS/MzLS (right). We can see that the most important imaging systematics are not the same depending on the region, which confirms the importance of treating the different surveys separately. In both regions, Galactic extinction (ebv) and the hydrogen atom column density (logHI) are important, such Galactic depths, airmass and sky brightness but in different bands depending on the region.

After identifying the most important imaging attributes, we derived a new set of photometric weights that account for the feature selection. In Fig. A2, we compare the projected cross-correlation function after applying this new set of NN weights (NN-FS) with our baseline where the feature selection was not applied. The top panel corresponds to BASS/MzLS in the eBOSS footprint and the bottom panel to DECaLS-South, for the redshift range $0.8 \leq z \leq 1.5$. The effect of including the feature selection is marginal and we found the same behaviour for $0.6 \leq z \leq 1.2$. For this reason, we kept the baseline to be the one without feature selection. We also check the consistency in terms of BAO constraints and the results when including the feature selection are shown in Table 3.
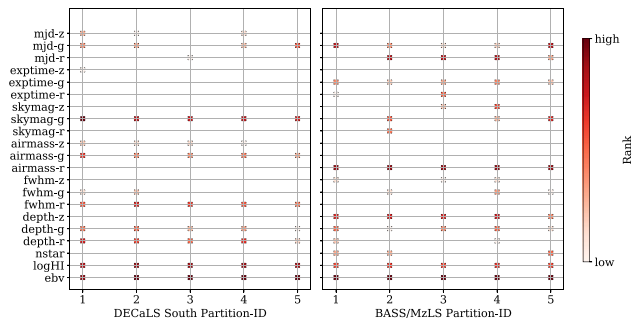

Figure A1. Important imaging maps according to the feature selection procedure for DECaLS-South (left) and BASS/MzLS (right). The selected maps are shown with circles and their rank is colour coded to represent the more important maps with the darker circles.
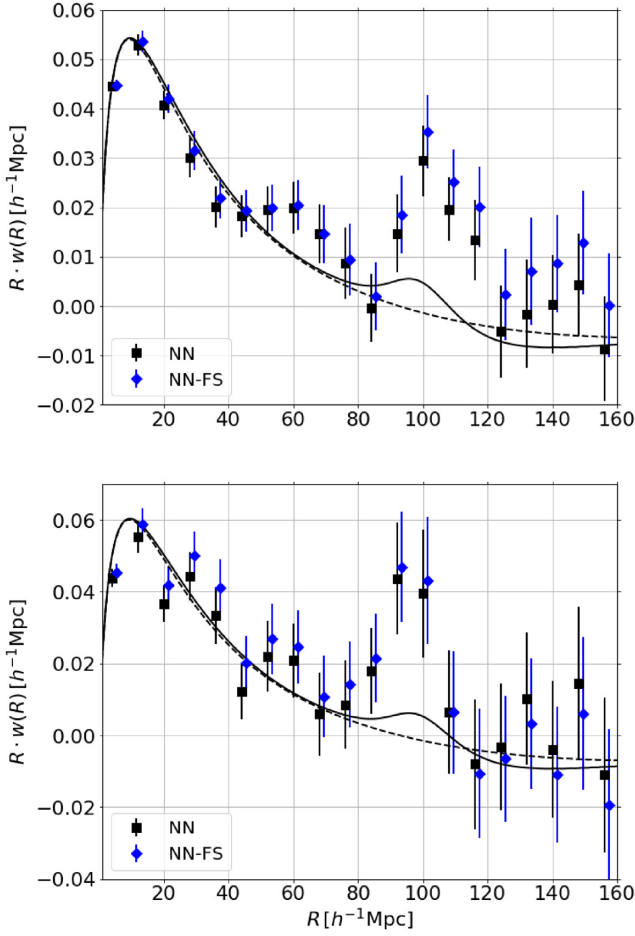
Figure A2. Projected cross-correlation function in $0.8 \leq z \leq 1.5$ in the BASS/MzLS (top) and DECaLS-South (bottom) regions after applying NN with feature selection (blue) and without (black, our baseline).

APPENDIX B: IMPACT OF MIXING DIFFERENT IMAGING SURVEYS

In what follows, in order to avoid mixing the surveys and because the analysis is limited to the eBOSS footprint, we remove the region at dec < 32.375 deg in both the spectroscopic and photometric samples to consider BASS–MzLS only in the NGC. We also remove the DES region in the SGC (dec < 5 deg) as it is deeper than DECaLS. Given that we restrict to the eBOSS footprint, the removed regions have small areas so the statistical precision is only slightly affected but in this section, we show that mixing these surveys degrades the cosmological signal significantly.

In Section 3.2, we describe the different imaging surveys we use to select the photometric sample and we show that the observed galaxy density correlates with imaging systematics differently depending on the survey. When we restrict to the eBOSS footprint, the NGC contains both BASS/MzLS at dec > 32.375 deg and DECaLS-North below while the SGC contains both DECaLS and DES at dec < 5 deg. In the main analysis, we decide to remove DECaLS-North in the NGC and DES in the SGC. Fig. B1 displays the impact on the projected cross-correlation function of removing those regions in the NGC (top) and in the SGC (bottom). In all cases, we show the projected cross-correlation function after applying the NN weights.

The measurements in blue correspond to the ones used in the main analysis when considering BASS/MzLS only in the NGC and DECaLS-S only in the SGC. We can see that the signal is largely improved when we consider BASS/MzLS only in the NGC. The effect of removing DES is less pronounced.

Fig. B2 displays the correlation matrix of the projected cross-correlation function obtained from the 100 jackknife regions for BASS/MzLS only (top) and for the entire eBOSS NGC (bottom). It seems that mixing the different surveys in the North brings inhomogeneities in the photometry that degrade the cosmological signal. Treating the DESI imaging surveys separately is therefore essential to preserve the cosmological information. Moreover, given that the main DESI ELG selection is also pushed towards faint magnitudes, there is an important ongoing effort within the DESI collaboration to study the impact of heterogeneous photometry on the clustering of these faint galaxies. The DESI ELG EZ mocks presented in Section 5.1.2 have been developed with this purpose in mind, in order to perform BAO and Full-Shape analyses on these mocks and quantify the effect on the cosmological parameters.
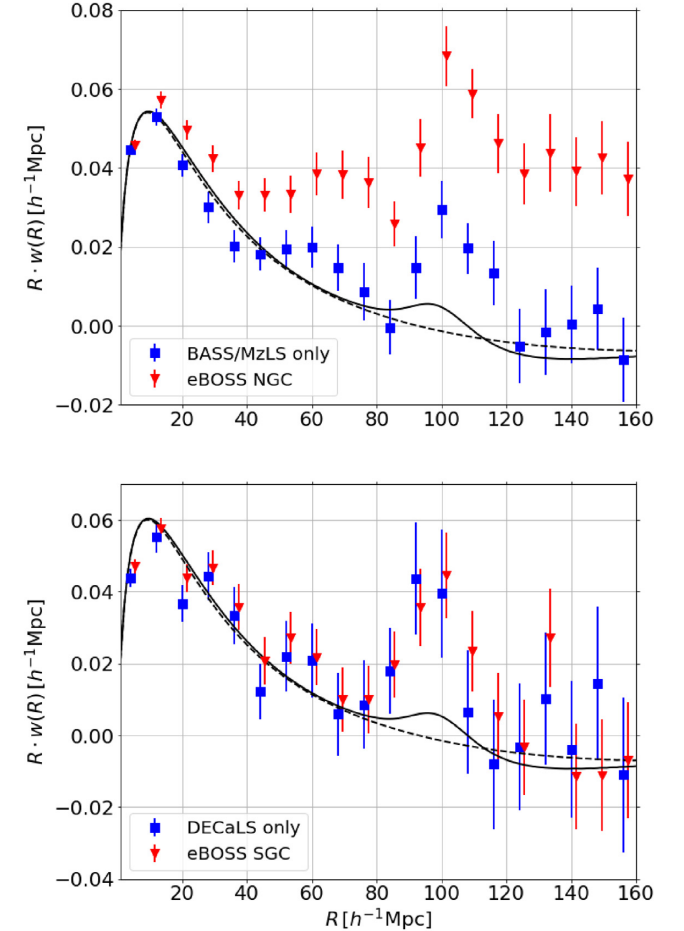

Figure B1. Impact of removing DECaLS-North in the eBOSS NGC (top) and DES in the eBOSS SGC (bottom) on the projected cross-correlation function. The measurements used in the main analysis correspond to the ones in blue. The cosmological signal is more degraded in the NGC as we combine different imaging surveys using different observing sites (BASS/Mzls and DECaLS) while in the SGC, we are using the same imaging camera but DES goes deeper than DECaLS.
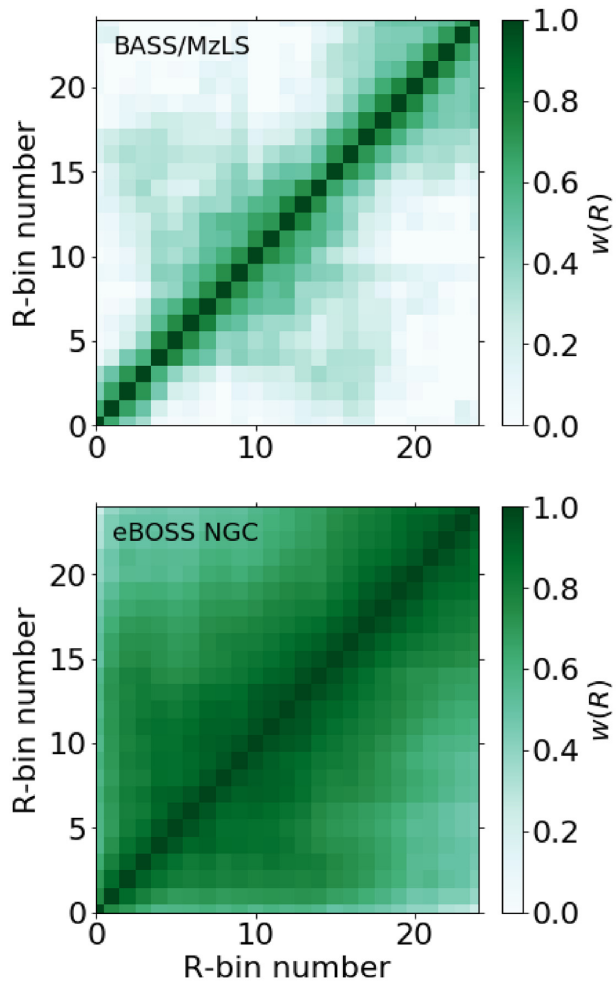
Figure B2. Correlation matrix of the projected cross-correlation function obtained from the 100 jackknife regions for BASS/MzLS only in the eBOSS NGC footprint (top) and for the entire eBOSS NGC (bottom) with two different imaging surveys, BASS/MzLS and DECaLS.

This paper has been typeset from a TEX/LATEX file prepared by the author.